

Strong coupling and single-photon nonlinearity in free-electron quantum optics

Aviv Karnieli^{1,‡,*}, Charles Roques-Carnes^{1,‡,†}, Nicholas Rivera², and Shanhui Fan¹

¹ *E. L. Ginzton Laboratories, Stanford University, 348 Via Pueblo, Stanford, CA USA*

² *Department of Physics, Harvard University, Cambridge, MA 02138, USA and*

[‡] *These authors contributed equally to the work.*

The observation that free electrons can interact coherently with quantized electromagnetic fields and matter systems has led to a plethora of proposals leveraging the unique quantum properties of free electrons. At the heart of these proposals lies the assumption of a strong quantum interaction between a flying free electron and a photonic mode. However, existing schemes are intrinsically limited by electron diffraction, which puts an upper bound on the interaction length and therefore the quantum coupling strength. Here, we propose the use of “free-electron fibers”: effectively one-dimensional photonic systems where free electrons co-propagate with two guided modes. The first mode applies a ponderomotive trap to the free electron, effectively lifting the limitations due to electron diffraction. The second mode strongly couples to the guided free electron, with an enhanced coupling that is orders of magnitude larger than previous designs. Moreover, the extended interaction lengths enabled by our scheme allows for strong single-photon nonlinearities mediated by free electrons. We predict a few interesting observable quantum effects in our system, such as deterministic single-photon emission and complex, nonlinear multimode dynamics. Our proposal paves the way towards the realization of many anticipated effects in free-electron quantum optics, such as non-Gaussian light generation, deterministic single photon emission, and quantum gates controlled by free-electron–photon interactions.

INTRODUCTION

The study of interactions between flying free electrons and quantized systems, such as electromagnetic fields or bound electrons, has led to the emerging field of *free-electron quantum optics* [1–8]. Free-electron quantum optics provides a promising platform for the generation of nonclassical light [1, 2, 4, 8–11], quantum information processing [12–16], and quantum sensing [2, 3, 5, 6, 17–20]. Specifically, measurement of free electrons’ energy can be used for the heralded generation of quantum light, such as Fock states [1, 4, 8, 10, 21], squeezed states [22] and even cat and GKP states [9]. More recently, it was predicted that free electrons could serve as ancillary qubits for quantum computation [15, 16], and provide a platform for nonlinear electron dynamics [23, 24] and deterministic single-photon nonlinearities [11, 25–27] owing to quantum recoil [28, 29].

Such free-electron-induced nonlinearities could become a potential resource for quantum nonlinear optics [30]. Unlike bound-electron systems, the vast spectral range spanned by free electron emitters (from THz [31] to x-ray [32]), their phase-matching bandwidth allowing robustness to cavity detunings [15], as well as their ability to image systems with femtosecond temporal resolution and sub-nanometer spatial resolution [33–35], may allow new paradigms in quantum optical technologies.

In order to realize the above-mentioned advancements, one needs strong free-electron–photon coupling and, sometimes, strong free-electron induced nonlinearities, ideally in a lossless dielectric structure. Free-electron–photon coupling is quantified by the dimensionless parameter g_Q , where $|g_Q|^2$ dictates the total number of photons that can be emitted by an electron phase-matched

to electromagnetic field modes. The condition $|g_Q| > 1$ is considered as the strong coupling regime. Recent experiments reported values of $|g_Q| \approx 1$ in electron-plasmon interactions [10] and $|g_Q| \approx 0.1$ in dielectric resonators [8, 36], while theoretical proposals have further considered waveguide geometries [37, 38] reaching similar values. Free-electron-induced nonlinearity, on the other hand, results from the fact that an electron’s velocity changes as it absorbs or emits photons [28, 29], an effect which can suppress or enhance subsequent photon emission by the same electron, due to modification of energy-momentum conservation [11, 25], the so-called *quantum recoil* correction [28]. The nonlinearity is characterized by a nonlinear phase δ_{NL} , where the condition for strong nonlinearity is $\delta_{\text{NL}} \sim 2\pi$. The quantum recoil correction has only been recently observed in the x-ray [29], while in the visible-IR range, such free-electron-induced nonlinearity has only been considered theoretically for very low energy electrons (e.g., $\leq 1\text{keV}$ kinetic energy) [11, 25], which introduces many additional experimental challenges which are yet to be overcome.

The ultimate factor limiting both the coupling strength $|g_Q|$ and the nonlinear phase δ_{NL} is the *finite interaction length*, L_{int} , between the free electron and the photon. While there are several practical factors hampering the interaction length in experiments, such as beam-sample alignment and sample charging, there exists a fundamental limitation due to electron beam diffraction, which causes the electron to eventually collide with the structure (after such collision, the electron is absorbed in the material and thereby lost, whereas incoherent light emission through electron-matter interaction can become dominant [39]). From simplified geometric arguments (Fig. 1(a)), the interaction length is proportional to $2h/\theta$,

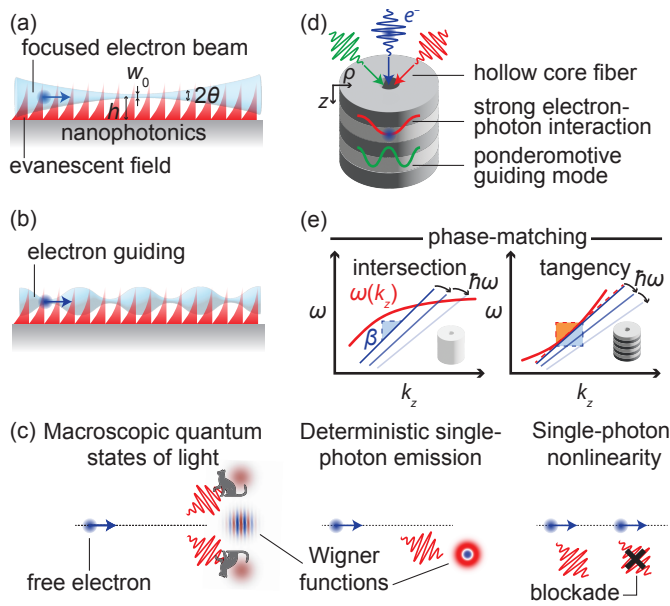


FIG. 1: **Enhanced free-electron-light interactions via ponderomotive guiding.** (a) In conventional free-electron-light interactions, the electron diffraction sets an upper bound on the electron mean free path, and consequently, on the interaction strength. (b) Using ponderomotive electron guiding, one can increase the electron mean free path by counteracting diffraction, resulting in enhanced interaction strengths. (c) Applications of strong interactions between free electrons and light. Representative Wigner functions and input-output pulses are shown for illustration. (d) Schematic of free-electron interactions with modes of an optical fiber providing guiding and strong free-electron-photon interaction. (e) Two schemes for phase-matching: intersection phase-matching in uniform fibers (left) and tangential phase-matching in Bragg fibers (right). The faded lines show the influence of photon emission on detuning.

where h is the beam position above the structure and θ its divergence angle, which vanishes as the electron velocity decreases (see Appendix A). Unfortunately, the latter observation can seriously hamper the realization of free-electron-induced nonlinearity effects: especially in experiments with low electron energies [40, 41]. Thus, venturing into the regimes of strong coupling and single-photon nonlinearity requires a significant increase in interaction lengths across a vast range of electron energies.

In this work, we propose a general method to achieve both strong free-electron-photon coupling and large free-electron-induced nonlinearity on the single-photon level in all-dielectric systems with extended interaction lengths. Key to our proposal is the use of hollow-core nanofiber (HCNF) and waveguide geometries that simultaneously support a ponderomotive guiding field, enabling long interaction lengths of the order of centimeters (Fig. 1(b)). This method allows us to predict record-high coupling values reaching $|g_Q| = 16.07$ (corresponding to over 250 photons emitted per electron) for transmission

electron microscopy (TEM) energies ($E = 200$ keV). For scanning electron microscopy (SEM) electron energies ($E = 17.8$ keV), and using Bragg HCNFs, we show that in addition to strong coupling ($|g_Q| = 2.77$), we predict a large nonlinear phase shift of $\delta_{NL} \approx 16\pi$, even for electron energies well-exceeding 1 keV and for a photon energy of 2.93 eV. This effect stems from an exceptionally-high Kerr-like nonlinearity emergent in our system Hamiltonian, as well as the long interaction length. We show that the proposed system demonstrates favored emission of photons into a single guided mode family. We then analyze the multimode, quantum-optical dynamics in our system, and identify experimental observables that unveil the single-photon blockade effects. Our results pave the way towards new capabilities in quantum optics, from macroscopic nonclassical light generation to room-temperature, electron-mediated single-photon nonlinearities (Fig. 1(c)).

We recently became aware of several related works [45–47] on the free-electron-photon quantum coupling, that have come out in parallel to this work.

HOLLOW-CORE NANOFIBERS AND WAVEGUIDES AS A PLATFORM FOR FREE-ELECTRON-LIGHT INTERACTIONS

Quantum optics in hollow-core fibers and slot waveguides is a well-established field, where the main focus has been on atomic emitters, positioned or trapped inside the hollow core or slot [48–51]. For free electrons, methods for guiding electron beams inside microwave ponderomotive waveguides [52, 53], free space [54], or dielectric laser accelerators [55–58] have been proposed and implemented. In the latter case, the aim of electron guiding is to mitigate the effect of acceleration-induced diverging forces acting on the electrons (which do not occur in the settings considered in this paper). To the best of our knowledge, electron guiding has never been proposed for the enhancement of quantum light emission and single photon nonlinearity, as detailed in this work.

We consider the two structures presented in Fig. 1(d), consisting of either a uniform HCNF, with inner radius a , outer radius b and refractive index n ; or a Bragg HCNF, with refractive indices n_1, n_2 , a periodicity Λ and duty-cycle D . Uniform HCNFs are more suitable for higher electron energies (above 80 keV, as in TEMs), whereas periodic structures enable us to extend the range of efficient coupling to lower electron energies (down to few-keV, as in SEMs), by slowing down the phase velocity of light [35, 59]. These two examples also allow us to investigate two different types of free-electron-photon phase matching, as illustrated in Fig. 1(e): the conventional case of an *intersection* point between the electronic and photonic dispersion curves [defined, respectively, by the RHS and LHS in Eq. (2)], and the previously unexplored

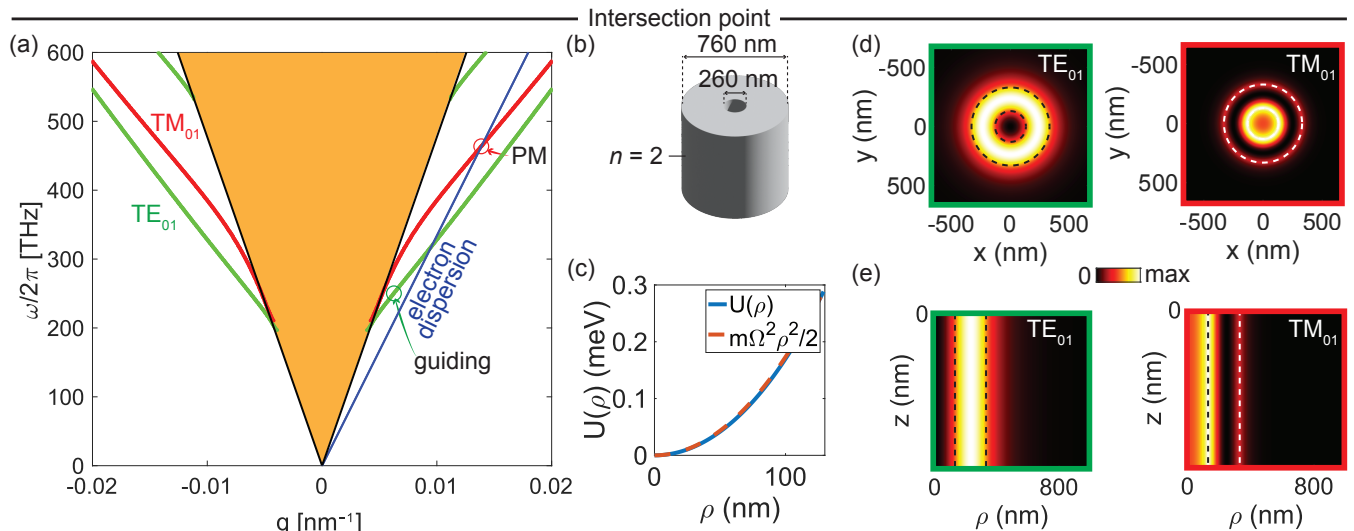


FIG. 2: **Intersection phase-matching in free-electron ponderomotive guiding.** (a) TE and TM band structure of a uniform hollow-core nanofiber design. (b) Schematic of the corresponding design. (c) Corresponding ponderomotive potential from the TE mode with peak pump power $P_0 = 30$ W. (d) Transverse cross sections of mode profiles for TE ($|E_\varphi|$) and TM ($|E_z|$) modes. (e) Longitudinal cross sections of mode profiles for TE ($|E_\varphi|$) and TM ($|E_z|$) modes. In (d) and (e), dashed lines indicate inner and outer fiber boundaries. PM: phase matching. Parameters used in the calculation are $n = 2$ (achievable with tellurite glass [42–44]); $a = 180$ nm, $b = 380$ nm, and electron energy $E = 200$ keV.

case of a *tangency* point. As we show below, the scaling of the coupling strength $|g_Q|$ with the interaction length and the nature of the single-photon nonlinearity will significantly differ between these two configurations.

HCNFS support several guided mode families [51]: TM modes, with a purely transverse magnetic field, TE modes, with a purely transverse electric field, and HE and EH hybrid modes, where both electric and magnetic fields have longitudinal components. Note that TM, HE and EH modes all have longitudinal electric field components. TE modes on the other hand, have zero longitudinal electric field components. The modes are typically labeled by indices l, p , standing for the orbital angular momentum (OAM) number and their radial number, respectively. Fig. 2(a,b) present the TM₀₁ and TE₀₁ bands of a uniform hollow nanofiber, together with the electron dispersion line (see simulation parameters in the caption of Fig. 2 and Appendices C and D). Mode profiles corresponding to the highlighted points on each band are presented in Fig. 2(d,e). The second HCNF design we study in this paper is shown in Fig. 3. Fig. 2(a,b) present its band diagram, inside the first Brillouin zone, of a Bragg HCNF. TE₀₁ and TM₀₁ mode profiles, corresponding to the highlighted points in Fig. 3(a), are presented in Fig. 3(d,e).

Below, we outline the essential properties of our proposed system, and how they enable the enhancement of free-electron–photon coupling, single photon nonlinearity, and β -factor. This is achieved through the ponderomotive guiding enabled by the TE₀₁ mode, simultane-

ously with the strong coupling with the TM₀₁ mode.

PONDEROMOTIVE GUIDING OF FREE ELECTRONS IN HCNFS

We consider a free-electron wavepacket propagating inside the hollow core, while being guided by a co-propagating trap potential: an intense laser pulse occupying the TE₀₁ mode supported by the structure (see Figs. 2(c) and 3(c) for TE₀₁ mode profiles). The guiding potential is induced through the elastic ponderomotive interaction (the A^2 term in the minimal-coupling Hamiltonian) felt by the electron, and, inside the hollow core $\rho < a$ (a is the radius of the hole), takes the form:

$$U_p(\rho) = \frac{e^2}{m_e \omega_{\text{TE}}^2} |E_{\text{TE}}(\rho)|^2 \approx \frac{1}{2} m_e \Omega^2 \rho^2 \quad (1)$$

where e, m_e are the electron charge and mass, respectively, and $\omega_{\text{TE}}, E_{\text{TE}}$ are the TE frequency and electric field, respectively. The radial dependency of the electric field of the chosen TE₀₁ mode is given by the first-order Bessel function $J_1(\zeta\rho)$ for $\rho < a$, where ζ is a complex vacuum transverse wavevector. Thus, for $|\zeta a| \ll 1$, Eq. (1) is well approximated by a 2D parabolic potential, as given by the right hand side, with $\hbar\Omega$ denoting the ground state energy (the parabolic fitting is shown in Figs. 2(c) and 3(c)). As a result, a set of guided electron wavefunctions can be supported by the structure, with the fundamental Gaussian mode $\psi_{0,0}(\rho)$ having spatial

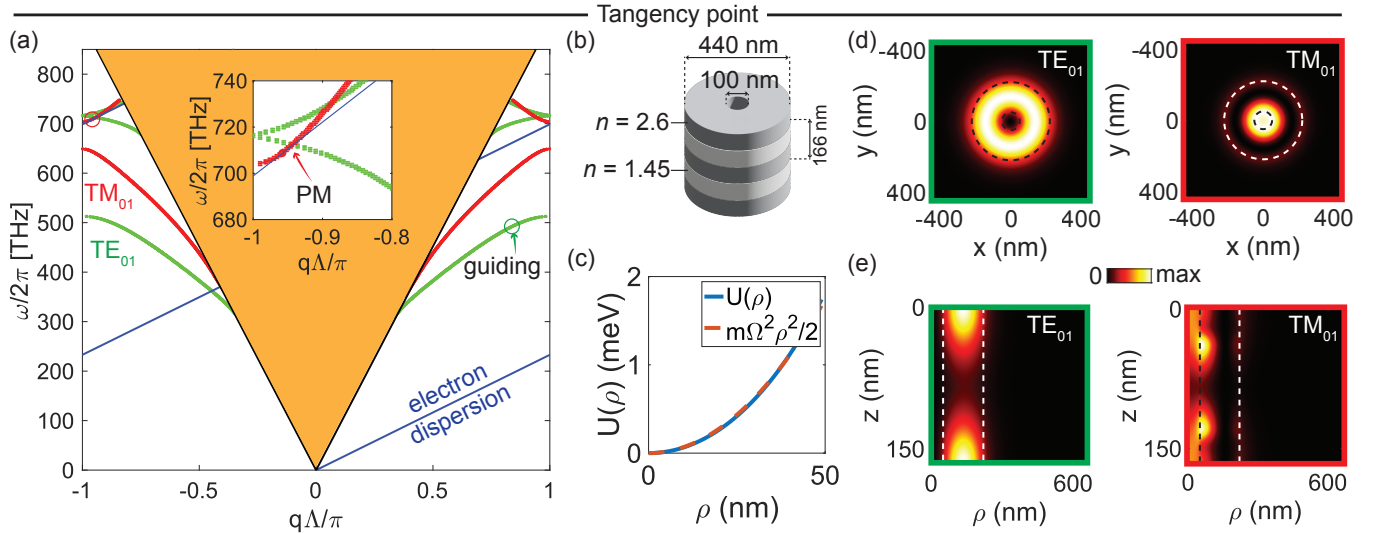


FIG. 3: **Tangency phase-matching in free-electron ponderomotive fiber guiding.** (a) TE and TM band structure of a hollow Bragg nanofiber design. (b) Schematic of the corresponding design. (c) Corresponding ponderomotive potential from the TE mode with peak pump power $P_0 = 500$ W. (d) Transverse cross sections of mode profiles for TE ($|E_\varphi|$) and TM ($|E_z|$) modes. (e) Longitudinal cross sections of mode profiles for TE ($|E_\varphi|$) and TM ($|E_z|$) modes. In (d) and (e), dashed lines indicate inner and outer fiber boundaries. PM: phase matching. Parameters used in the calculation are $a = 50$ nm, $b = 220$ nm, $\Lambda = 165.7$ nm, $D = 32.48\%$, with $n_1 = 2.6$ (achievable with SiC nanophotonic waveguides [60] or chalcogenide glass nanofibers [61]), $n_2 = 1.45$ (using SiO₂ or, alternatively, air corrugations), and electron energy of $E = 17.8$ keV. Note that, in the periodic case, the electron dispersion line in (a) wraps around the Brillouin zone.

uncertainty $\Delta r_e = \sqrt{\hbar/2m_e\Omega} \ll a$. Higher-order guided wavefunctions, $\psi_{l,p}(\rho)$ can also be supported.

Assuming the electron and trap pulse co-propagate, classical theory predicts that a portion of the electron phase-space trajectories can be guided indefinitely; this is in contrast to the non-guided case where almost all electrons eventually hit the structure walls. Considering a quantum treatment, where electrons can also tunnel outside the trap into the surrounding material, the mean free path of the guided electron mode can be calculated using leaky-mode theory (see Appendix B). The resulting tunneling mean free path can still be orders of magnitude larger than other relevant limiting length scales, such as the propagation loss length, or the group-velocity mismatch (GVM) length, $L_{\text{GVM}} = \tau/|1/v_g - 1/v_e|$, between the electron (velocity v_e) and the trap (group velocity v_g , pulse length τ). Therefore, in our example structures, we choose to limit the interaction lengths according to the latter quantities. The chosen parameters for the TE ponderomotive trap, for each of the examples in this work, are outlined in Appendix C.

STRONG FREE-ELECTRON-PHOTON COUPLING WITH LARGE β -FACTORS

The free electron guided by the ponderomotive potential, as discussed in the previous section, can be used

to achieve strong free-electron-photon coupling. For this purpose, the photon must be in a mode that supports a longitudinal electric field component, and therefore, must be in either the TM, HE or EH mode families. Achieving strong free-electron-photon coupling typically requires satisfying the phase-matching condition

$$\omega(q) = \frac{E(k) - E(k - q - 2\pi m/\Lambda)}{\hbar}, \quad (2)$$

which is a resonance condition between the electron and photon enabling efficient exchange of energy. In Eq. (2), $E(k)$ is the electron energy at momentum $\hbar k$, $\omega(q)$ is the photonic dispersion relation, q is the photonic wavevector in the waveguide, and m is an integer. For a uniform system, $m = 0$, while for a periodic system, m corresponds to the number of times the electron dispersion wraps around the Brillouin zone (Fig. 3(a)). Graphically, a solution $(q, \omega(q))$ to Eq. (2) corresponds to a phase-matching point where the electron dispersion curve crosses a photonic band. The two types of phase-matching points, illustrated in Figs. 2 and 3, are obtained for the two types of structures: for the uniform HCNF, we have an intersection point with the TM₀₁ mode (highlighted in Fig. 2(a)), for zeroth-order ($m = 0$) phase-matching. For the Bragg structure, we obtain a tangency point at the bottom of the TM₀₁ upper band (highlighted in Fig. 2(f) and its inset), using second-order ($m = 2$) phase-matching.

Strong free-electron-photon coupling manifests as in-

elastic scattering (i.e., exchange of many quanta of energy and momentum) between the electron and incident quantum light. If no light is initially present, strong coupling corresponds to the spontaneous emission of photons by a single electron [1, 2, 10]. The latter scenario will be the focus of this work, as it can be used for shaping and heralding of quantum states of light [4, 8, 9, 37]. In the linear regime ($\delta_{\text{NL}} \ll 2\pi$), each electron emits on average $|g_Q|^2$ photons, in a Poissonian distribution, while in the nonlinear regime $\delta_{\text{NL}} \gg 2\pi$, we should expect a sub-Poissonian distribution, and vacuum Rabi oscillations as a function of $|g_Q|$ [11].

We calculate the total coupling efficiency to a general mode family (labeled by $s = \text{TM}_{ij}, \text{TE}_{ij}, \text{HE}_{ij}$), for m -th order phase-matching and for the two types of phase-matching points, as

$$|g_{Q,s}|^2 = \frac{\alpha}{\tilde{A}} \frac{L_{\text{int}}}{\lambda} \left| \int d^2\rho \psi_f^*(\rho) \psi_i(\rho) u_{m,z}^{(s)}(\rho) \right|^2 \times \begin{cases} 1/|1 - v_{g,s}/v_e| & \text{intersection} \\ (4/3\sqrt{\pi}) \sqrt{L_{\text{int}}/v_{g,s}^2|\beta_2|} & \text{tangency,} \end{cases} \quad (3)$$

where $\alpha \approx 1/137$ is the fine structure constant, $\tilde{A} = A/\lambda^2$ is the normalized mode area, and λ is the free-space wavelength of the mode. Here, $\mathbf{u}_m(\rho)$ is the m -th Fourier component in the expansion of the mode function (a Bloch function in a periodic system), written as $\mathbf{u}(\mathbf{r}) = \sum_m \mathbf{u}_m(\rho) e^{i2\pi m z/\Lambda}$. The normalization of $\mathbf{u}(\mathbf{r})$ is such that $\mathbf{E}(\mathbf{r}) = \sqrt{\hbar\omega(q)/2\epsilon_0 A} e^{iqz} \mathbf{u}(\mathbf{r})$. $\psi_{i/f}$ denote the initial and final free-electron transverse wavefunctions (here, unless stated otherwise, $\psi_i = \psi_{00}$ is the fundamental mode). Finally, v_e is the electron velocity, and β_2 is the group velocity dispersion at the phase-matching point. More details on the derivation are provided in Appendix D.

From the form of Eq. (3), it is clear that modes with high transverse confinement $\tilde{A} \ll 1$ and large overlap with the electron wavefunctions are favored. The type of phase-matching point quantifies the effective number of longitudinal (spectral) modes within the phase-matching bandwidth. Interestingly, this further implies different scalings of $|g_Q|^2$ with respect to the interaction length: $|g_Q|^2 \propto L_{\text{int}}$ for an intersection point, and $|g_Q|^2 \propto L_{\text{int}}^{3/2}$ for a tangency point. Fig. 4 shows the different scaling and achievable values of coupling with reasonable experimental parameters. The combination of strong transverse confinement and large overlap of the TM01 mode, together with the guiding-enhanced interaction lengths, enables exceptionally high predicted coupling values of $|g_{Q,\text{TM}}| = 16.07$ and $|g_{Q,\text{TM}}| = 2.77$, for the uniform and Bragg examples, respectively.

Another important figure of merit is the β -factor, extensively used in waveguide quantum electrodynamics [62], defined as the ratio between the coupling to the

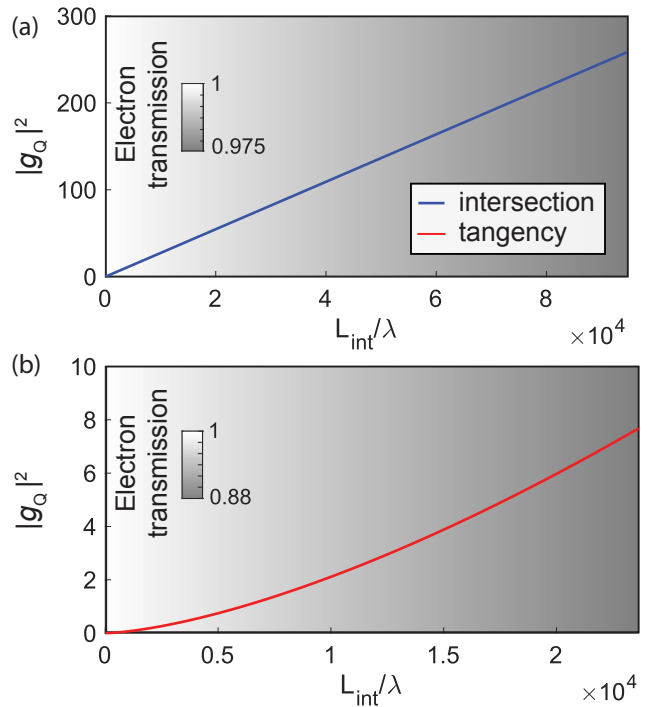


FIG. 4: **Electron-photon coupling: scaling and physical limits.** Scaling of the free-electron-photon coupling as a function of the interaction length is shown for intersecting phase-matching (top, blue) and tangency phase-matching (bottom, red). Background color corresponds to the electron transmission probability calculated according to Appendix B with $-2\text{Im}(2p+1) = 10^{-3}$.

desired mode (here, TM01), to the total coupling:

$$\beta = \frac{|g_{Q,\text{TM01}}|^2}{|g_{Q,\text{TM01}}|^2 + \sum_{s \neq \text{TM01}} |g_{Q,s}|^2}, \quad (4)$$

where the modes $s \neq \text{TM01}$ are all other modes the electron may couple to. Since the TM01 mode is the only one to have a non-zero amplitude at the center of the hollow core, it most efficiently couples to the free electron. Moreover, when the electron wavefunction is spatially confined ($\Delta r_e \ll a$), an electron transition where $\psi_f = \psi_i = \psi_{00}$ is strongly favored. The electron also excites HE and EH modes, as these carry an E_z component, which is along the propagation direction of the electron. However, such modes possess orbital angular momentum (OAM), with a singularity at the center of the hollow core. This will reduce the overlap with the transverse electron wavefunction, and further requires that the electron exchanges an OAM quantum with the field. Thus, ψ_f must have a nonzero OAM quantum number, whereas its largest overlap with $\psi_i = \psi_{00}$ happens for a radial number $p = 0$. Eventually, this overlap can be made arbitrarily small using stronger electron transverse confinement. Thus, we can ensure that the β -factor approaches unity, even when the coupling efficiency is arbitrarily increased [79]. In our

examples, we find β -factors of 0.89 (resp., 0.99) for the uniform (resp., Bragg) designs. For the Bragg design, coupling to $l \neq 0$ modes is further suppressed by the strongly-decaying evanescent fields that accompany the nonzero Fourier components of the Bloch functions.

KERR-LIKE HAMILTONIAN AND SINGLE-PHOTON NONLINEARITY ENABLED BY FREE ELECTRONS

In the previous sections we have seen how extending the interaction length via electron guiding can dramatically increase the coupling. Intriguingly, an extended interaction enables us to enter a completely different physical regime where quantum recoil corrections [29] can manifest as a *single photon nonlinearity* mediated by free electrons.

The physical intuition for this phenomenon is as follows: for swift electrons and short interaction lengths, the electron experiences no recoil (or back-action) by an emitted photon. Thus, an electron already phase-matched to an optical mode remains phase-matched even after emitting a photon, and can, therefore, continue emitting more photons. The interaction length is assumed to be short enough such that even if such recoils do occur, they do not accumulate to any significant effect.

However, the situation is very different when we consider slower electrons and long interaction lengths: slower electrons can experience a non-negligible recoil after the emission of even a single photon, such that after the emission their momentum has changed. This results in an electron detuning from the optical mode (e.g, if the electron was originally phase matched, after emitting one photon, it is no longer phase matched): and in that case, the longer the interaction length, the larger the effect this detuning has on a consecutive emission of a second photon. In the limit where the detuning-induced phase mismatch accumulated along the interaction becomes very large, the electron cannot emit a second photon at all.

To elucidate this single-photon nonlinearity mediated by free electrons, we first write the non-relativistic free-electron-photon interaction Hamiltonian as

$$H = \frac{p^2}{2m} + \sum_q \hbar\omega_q a_q^\dagger a_q + \sum_q \hbar\Omega_q (a_q b_q^\dagger + a_q^\dagger b_q), \quad (5)$$

where p is the electron momentum, $\Omega_q = ev_0 \sqrt{\hbar/2\epsilon_0\omega_q V}$ is the coupling constant for each mode (satisfying $|g_Q|^2 = \sum_q |\Omega_q|^2 \text{sinc}(\Delta_q L_{\text{int}}/2v)$, with the detuning Δ_q defined below), and $b_q = e^{-iqz}$ is the electron momentum ladder operator, with $[b_q, b_{q'}^\dagger] = 0$ [1]. In Appendix F, we show that in a subspace with a fixed total momentum P , this Hamiltonian can be recast into the form of an effective

Kerr nonlinearity acting on an effective photon:

$$H_{\text{eff}} = \sum_q \hbar\Delta_q A_q^\dagger A_q + \sum_q \hbar\Omega_q (A_q + A_q^\dagger) + \hbar\kappa N(N-1), \quad (6)$$

where $\kappa = \hbar q_0^2/2m$ is the effective Kerr nonlinearity around the phase-matching point (q_0, ω_0) , and

$$\Delta_q = \omega_q - qv + \frac{\hbar q^2}{2m} \quad (7)$$

denotes the free-electron-photon detuning. The total excitation number is given by:

$$N = \sum_q A_q^\dagger A_q. \quad (8)$$

In writing Eq. (6), we have introduced the hybrid ladder operators $A_q = a_q b_q^\dagger$, which act on a joint Hilbert subspace of the free electron and photons, spanned by the states $|P - n\hbar q\rangle_{\text{el}} |n_q\rangle_{\text{ph}}$, where $A_q |P - n_q \hbar q\rangle_{\text{el}} |n_q\rangle_{\text{ph}} = \sqrt{n_q} |P - (n_q - 1)\hbar q\rangle_{\text{el}} |n_q - 1\rangle_{\text{ph}}$. Using the commutation relations of b_q , we find that $[A_q, A_{q'}^\dagger] = \delta_{q,q'}$: these new operators have the same commutation relations as photon operators, and further satisfy $A_q^\dagger A_q = a_q^\dagger a_q$ (the latter holds for a single-electron system). With that in mind, we see that Hamiltonian Eq. (6) effectively describes a multimode bosonic system with a Kerr nonlinearity that couples to the total excitation number. For spontaneous emission, where the initial electron momentum is $p = mv$ and the electromagnetic field is initially at vacuum, a phase-matched electron could excite a (generally multimode) state. The Kerr term $\hbar\kappa N(N-1)$ ensures that any excitation number beyond $N = 1$ is detuned from phase matching, and in the limit where this detuning is large enough, we should expect a photon blockade where further light emission by the electron is suppressed.

The inherent multimode nature of the problem (namely, the summation over q in Eq. (6)) complicates the qualitative description we gave in the beginning of the section. In fact, in a continuous multimode system, such as the guided-wave structures considered here, the type of phase-matching point can significantly affect the dynamics. For example, for an intersection point phase-matching in a continuous case, a nonlinear detuning as in the Hamiltonian from Eq. (6) can indeed cause a considerable phase mismatch between the free electron and an initially emitted photon wavepacket. Graphically, the detuning is manifested as a change in the slope of the electron dispersion - since recoil changes the electron velocity - and as such, the electron dispersion no longer intersects the photon dispersion at the same point. However, as illustrated in Fig. 1(e) (left panel), there exists a continuum of other available intersection points. Thus, although high nonlinearity suggests that an electron tends

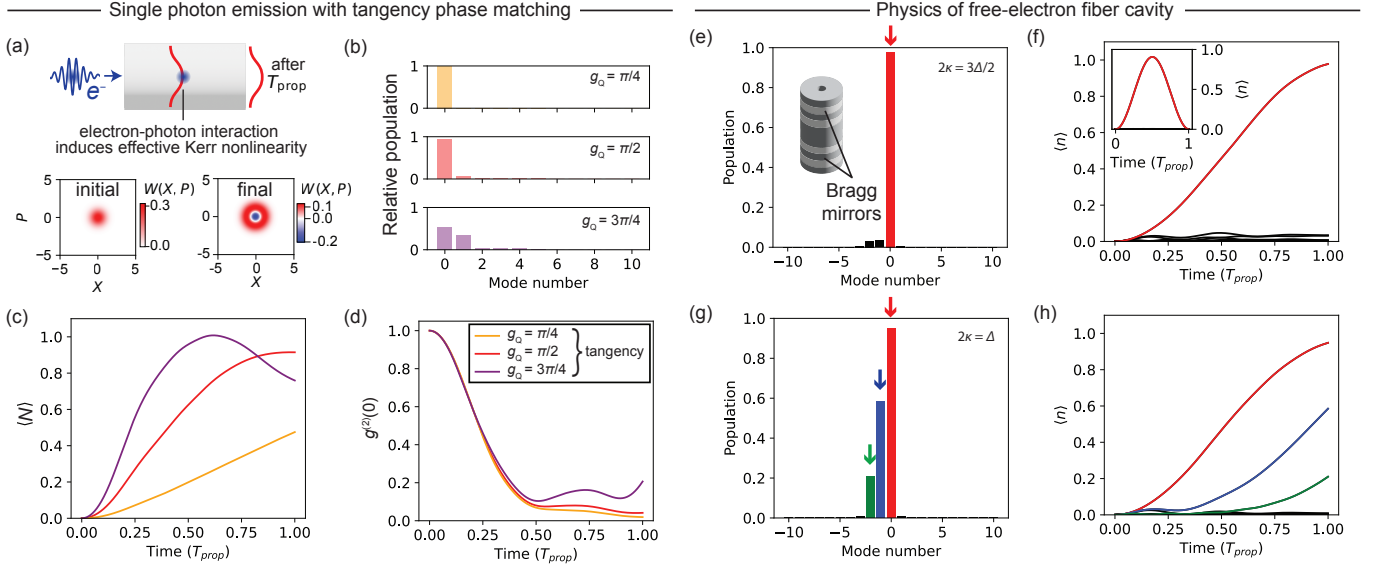


FIG. 5: Single-photon nonlinearity and cascaded photon emission in free-electron photonic fibers and fiber cavities. (a-d) Tangency phase matching. (a) Deterministic single photon emission in free-electron-photonic fiber interactions. Insets: initial state Wigner function (left); simulated final state Wigner function (right), for $|g_Q| = \pi/2$. (b) Simulated occupations on supermode basis, for different values of $|g_Q|$. (c) Time evolution of the total photon number for different values of $|g_Q|$ as in (b). (d) Time evolution of the second-order correlation function at zero-delay. (e-f) Single-photon nonlinearity in free-electron fiber cavities. (e) cavity mode population for $|g_Q| = \pi/2$ and $2\kappa = 1.5\Delta$ and $E = 3.72$ keV. (f) Time evolution of cavity mode photon numbers (with same parameters as in (e)), recovering the Jaynes-Cummings regime for $E = 3.72$ keV. Inset: For reference, the time evolution showing an almost ideal, full Rabi cycle for $|g_Q| = \pi$ and $E = 100$ eV is plotted. (g,h) Same as in (e,f) with $E = 3.72$ keV, but for $2\kappa = \Delta$, resulting in cascaded emission into consecutive cavity modes.

to not emit twice into the same mode, it can in fact continue emitting more photons into other modes, in a cascaded fashion. While this observation implies that a single-photon blockade effect is less likely to happen at a continuous intersection phase matching point, it can still be of practical use. For example, by partially filtering some of the modes, it may still be possible to obtain a photon-number state without post-selection of the electron energy.

The situation is very different if one considers instead a tangency phase-matching point: in this case, a single recoil leaves the electron dispersion curve below the photonic dispersion curve (Fig. 1(e), right panel), and thus the electron stays detuned from any other modes after a single excitation. We therefore focus our attention on this type of dynamics. We note, however, that the multimode nature of the dynamics still requires a more complicated treatment than in the linear regime, as the electron can interact with multiple *supermodes*: photonic wavepacket modes with different spectral (or temporal) shapes. In Appendix G, we develop a nonlinear supermode formalism that captures the dynamics in our system, and use it to calculate relevant experimental observables. We find that for values of g_Q as high as $\pi/2$ (a half vacuum-Rabi oscillation), the free electron mainly excites a single fundamental supermode, which allows us to further evaluate the resulting quantum state contained in that

supermode.

Figs. 5(a-d) depict simulation results for the tangency phase-matching point in the nonlinear regime, corresponding to the parameters of the tangency point example in Fig. 3 (see Appendix D for more details), and for different values of the total coupling $|g_Q|$. The predicted single-photon Kerr nonlinearity for this setup is $\kappa = 2\pi \times 30.06$ GHz, corresponding to a nonlinear phase $\delta_{NL} = 2\kappa L_{int}/v \approx 16\pi$. Fig. 5(a) shows the calculated Wigner functions occupying the fundamental supermode, for $|g_Q| = \pi/2$. As expected, the Wigner function shows a considerable negativity, and resembles that of a single-photon Fock state $W(\alpha) = (2/\pi) \exp(-2|\alpha|^2)(4|\alpha|^2 - 1)$, a donut-shaped distribution with a negative central dip. Fig. 5(b) shows the corresponding supermode populations for different values of $|g_Q|$, and Fig. 5(c) shows the time evolution of the expectation value of the total excitation number, for the same values of $|g_Q|$ as in Fig. 5(a,c). The total excitation number experiences a vacuum Rabi oscillation, though with limited visibility, owing to the excitation of other supermodes (interestingly, a similar behavior is obtained in the deep-quantum regime of multimode parametric downconversion [63]). Finally, Fig. 5(d) shows the value of the second-order correlation function at zero delay, $g^{(2)}(0) = \langle N(N-1) \rangle / \langle N \rangle^2$, as a function of interaction time and for different total coupling $|g_Q|$ (note that here we eval-

uate $g^{(2)}(0)$ with respect to the *total* excitation number N). A value of $g^{(2)}(0) \ll 1$ at the end of the interaction indicates that the system approximately remains in the single-excitation manifold, which is a hallmark of the expected single-photon nonlinearity. For $|g_Q| > \pi/2$, coupling to supermodes other than the fundamental decreases this effect. We emphasize that these strong nonlinear effects are obtained even for energies well-exceeding 1 keV (namely, 17.8 keV in this example), which are more experimentally accessible than the sub-keV energies that have been recently considered for quantum recoil effects [11, 23–27].

Interestingly, other regimes of interaction emerge if the photonic system hosts a discrete set of modes, e.g., as in a fiber cavity, which could be realized in our system by introducing Bragg mirrors at fiber ends (Fig. 5(e), inset). In this case, the electron dispersion can intersect the photonic modes only at certain, equally-spaced values. Now, when the electron experiences recoil following emission of a photon into cavity mode j , it may or may not be detuned from other neighbouring modes: this will strongly depend on the ratio between the recoil detuning 2κ and the effective spacing between the modes (defined in Eq. S48 in Appendix G), which we call the effective free spectral range and denote by Δ .

A specific choice of group velocity mismatch between the electron and cavity modes makes the cavity supermode basis coincide with the original set of cavity modes (more details can be found in Appendix G). In this manner, the fundamental supermode excited by the electron becomes a *single* cavity mode. Two distinct behaviors are depicted in Fig. 5(e-h). For a choice of nonlinearity $2\kappa = 1.5\Delta$, the electron excites a single cavity mode and is detuned from the rest, as can be seen in the cavity mode population (Fig. 5(e)) and the evolution of the average photon numbers (Fig. 5(f)), displaying a distinct vacuum Rabi oscillation. This is the so-called Jaynes-Cummings regime [11], where the electron reduces to an effective two-level emitter interacting with a single mode. Another choice, this time of $2\kappa = \Delta$, makes sure that following every recoil, the electron is always phase-matched to a neighboring mode. This results in a cascaded emission of photons into several cavity modes, as can be seen in the mode population (Fig. 5(g)) and photon number dynamics (Fig. 5(h)). We note again that these effects can occur at energies higher than 1 keV (3.72 keV in this example).

DISCUSSION AND OUTLOOK

We have shown that ponderomotive guiding in hollow-core photonic structures such as fibers and waveguides, could be used to increase the interaction length between free electrons and photons. As a result, we predict that such structures could strongly enhance both free-

electron–photon coupling and single-photon nonlinearities mediated by free electrons.

While several platforms are promising candidates to achieve strong free-electron–photon coupling [8, 10, 36–38, 64], these proposals are ultimately hampered by electron diffraction, limiting the interaction length between free electrons and photons. Ponderomotive guiding, on the other hand, can result in orders-of-magnitude increase in free-electron–photon coupling in either intersection or tangency phase matching designs. Tangency phase matching has the additional advantage of matching the group velocity of the free-electron wavepacket to that of the emitted photonic mode and that of the guiding field. In principle, one could also achieve group velocity matching between the electron and the guiding field, even in intersection phase matching, with appropriate dispersion engineering. This is favorable for increasing the interaction length and decreasing the required guiding optical fluence. Further, in our current design, the guiding field is mostly confined in the dielectric structure, which results in limited guiding power due to damage threshold of the material. Alternative designs employing dispersion engineering and allowing higher optical powers could rely, e.g., on air guiding in photonic crystal fibers [65, 66], thereby alleviating these limitations.

The long interaction lengths predicted in our designs would enable the realization of strong single-photon nonlinearities using free electrons. The designs proposed in this paper also rely on purely dielectric materials, thereby mitigating the effect of losses on quantum dynamics and coherence. The realization of single-photon nonlinearities with free electrons opens up many exciting prospects in free-electron quantum optics, such as the efficient and deterministic (or heralded) generation of non-Gaussian light. In the proposed system, owing to the availability of a large coupling coefficient g_Q , such effects can in principle be observed even after a single pass of a single free electron, instead of slower, multi-electron consecutive interactions previously considered in the literature [4, 9]. As we showed in Fig. 5, the strong nonlinearity induced by free electrons also results in complex multimode dynamics that are reminiscent of broadband parametric down conversion in the deep quantum regime [63].

While we expect that the realization of strong coupling between free electrons and photons to be an immediate application of our ponderomotive guiding design, it is worth noting that atomic emitters could also be integrated in the hollow core of the fiber [48–51]. With recent proposals highlighting the possibility of controlling atomic emitters with modulated electron beams [3], we expect that this platform could also be utilized to explore fascinating and complex quantum dynamics involving three flavors of interacting quantum systems: free electrons, photons, and atomic emitters [18, 67, 68].

APPENDIX A : GEOMETRICAL BOUND ON FREE-ELECTRON-PHOTON COUPLING STRENGTH

In this Appendix, we outline a simple geometric argument showing the limitation on the interaction length due to electron beam diffraction. From Fig. 1(a), we can estimate the interaction length as $L_{\text{int}} = 2h/\theta$. Since $|g_Q|^2 \propto L_{\text{int}} \exp(-2h/\lambda_{\text{ev}}) \propto h \exp(-2h/\lambda_{\text{ev}})$, where λ_{ev} is the evanescent wavelength, the optimal positioning of the e-beam above the sample is $h_{\text{opt}} = \lambda_e/2$. From phase-matching considerations, $q_z = \omega/v_e = 2\pi/\lambda\beta_e$ (with $\beta_e = v_e/c$), and $\sqrt{q_z^2 - q^2} = 1/\lambda_{\text{ev}}$, we can write $\lambda_{\text{ev}} = \beta_e\gamma_e\lambda/2\pi$ (with $\gamma_e = 1/\sqrt{1-\beta_e^2}$), and find that the interaction length is bounded by

$$\begin{aligned} L_{\text{int}} &= \frac{2h}{\theta} \leq 2\pi\beta_e\gamma_e \frac{hw_0}{\lambda_C} \\ &= \frac{\beta_e^3\gamma_e^3}{8\pi} \frac{\lambda^2}{\lambda_C} \left(\frac{h}{h_{\text{opt}}}\right) \left(\frac{w_0}{h_{\text{opt}}}\right), \end{aligned} \quad (\text{S1})$$

where the inequality holds for a Gaussian electron beam of waist w_0 , $\lambda_C = 2.426$ pm is the Compton wavelength, and we consider both w_0 and h relative to the optimal positioning h_{opt} . With diffraction, there is no obvious way to increase g_Q by increasing L_{int} : if we increase h to increase L_{int} , then $|g_Q|$ decays exponentially. Further, L_{int} quickly decreases with decreasing electron velocity β_e . Considering optimal positioning $h = h_{\text{opt}}$, a modest confinement of $w_0 = h_{\text{opt}}/2$ and $\lambda = 500$ nm, we have that $L_{\text{int}} = 2.1$ mm $\times \beta_e^3\gamma_e^3$. For the energies considered here, $E = 200$ keV ($\beta_e = 0.7$) and $E = 17.8$ keV ($\beta_e = 0.257$), we find that $L_{\text{int}} \leq 2$ mm and $L_{\text{int}} \leq 40$ μm , respectively.

APPENDIX B: FREE-ELECTRON MEAN FREE PATH IN PONDEROMOTIVE POTENTIAL

In this Appendix, we evaluate the mean free path for electron guiding with a finite parabolic potential. A classical electron trajectory analysis predicts that all electron trajectories with transverse kinetic energy less than or equal to the maximum value of the trap potential are guided indefinitely. However, in a quantum picture, free electrons may tunnel outside of the trap and into the surrounding bulk material. To evaluate the typical tunneling propagation length, we envision the equivalent optical problem of a leaky waveguide, and employ leaky mode theory [69]. For this we write the Schrödinger equation in cylindrical coordinates:

$$-\frac{\hbar^2}{2m} \left[\frac{\partial^2}{\partial z^2} + \frac{1}{\rho} \frac{\partial}{\partial \rho} \left(\rho \frac{\partial}{\partial \rho} \right) \right] \psi + V(\rho)\psi = E\psi, \quad (\text{S2})$$

with

$$V(\rho) = \begin{cases} \frac{1}{2}m\Omega^2\rho^2 & \rho \leq a \\ -eU & \rho > a \end{cases} \quad (\text{S3})$$

where $U > 0$ is the mean inner potential of the bulk material surrounding the hollow core.

In the absence of guiding ($\Omega \rightarrow 0$), we consider a worst-case scenario estimate, where an electron impinging on the wall at $\rho = a$ is fully transmitted and thereby lost. Thus, we set $U = 0$. In fact, choosing $U > 0$ will increase the mean free path, as this results in a nonzero reflection probability back into the hollow core, and can also be shown by numerically solving Eq. (S2). For simplicity, we solve the Schrödinger equation for radial modes without OAM, so we write $\psi(\rho, z) = e^{ik_z z}\phi(\rho)$, we find that ϕ satisfies:

$$\frac{1}{x} \frac{d\phi}{dx} + \frac{d^2\phi}{dx^2} + \left(2p+1 - \frac{x^2}{4}\Theta(\bar{a}-x) \right) \phi = 0 \quad (\text{S4})$$

where $x = \rho/\Delta r_e$ (with $\Delta r_e = \sqrt{\hbar/2m\Omega}$), $\bar{a} = a/\Delta r_e$, $2p+1 = (E - \hbar^2 k_z^2/2m)/\hbar\Omega$, and $\Theta(\bar{a}-x)$ is the Heaviside step function. The only solution that is non-divergent at $x = 0$ is of the form

$$\phi(x) = \begin{cases} Ae^{-x^2/4} L_p^0(x^2/2) & x \leq \bar{a} \\ BH_0^{(1)}(\sqrt{2p+1}x) & x > \bar{a}, \end{cases} \quad (\text{S5})$$

where $L_n^m(x)$ is the generalized Laguerre polynomial, and $H_0^{(1)}(x)$ is the Hankel function of the first kind. In the limit $\bar{a} \rightarrow \infty$, p is an integer, denoting the radial index of the guided mode. Otherwise, p is approximately an integer, and may have a small and negative imaginary part. Note that for non-integer orders, the Laguerre polynomials are also given by $L_n^0(x) = {}_1F_1(-n, 1, x)$. Requiring that ϕ and its derivative are continuous at $x = \bar{a}$, using $(L_n^0(x))' = -L_{n-1}^1(x)$ and $(H_0^{(1)}(x))' = -H_1^{(1)}(x)$, we find the dispersion relation for p :

$$\frac{1}{2} + \frac{L_{p-1}^1(\bar{a}^2/2)}{L_p^0(\bar{a}^2/2)} = \frac{\sqrt{2p+1}H_1^{(1)}(\sqrt{2p+1}\bar{a})}{\bar{a}H_0^{(1)}(\sqrt{2p+1}\bar{a})}. \quad (\text{S6})$$

We numerically solve Eq. (S6) by searching for its complex roots near $2m+1$, $m = 0, 1, 2, \dots$. Once found, we can evaluate the lifetime via:

$$k_z = \sqrt{\frac{2m}{\hbar^2} [E - \hbar\Omega(2p+1)]} \approx k_{z,0} - i\frac{\Omega}{v}\text{Im}(2p+1), \quad (\text{S7})$$

such that

$$\Lambda_{\text{MFP}}^{-1} = 2\text{Im}k_z \approx -\frac{2\Omega}{v}\text{Im}(2p+1). \quad (\text{S8})$$

A similar expression could be obtained using the WKB approximation, where $-\text{Im}(2p+1)$ is interpreted as a tunneling probability, and $2\Omega/v$ is the frequency (in units

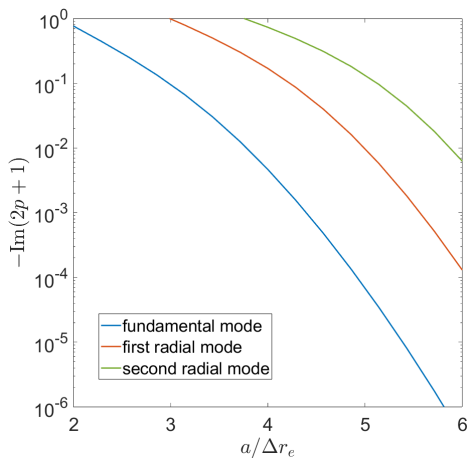


FIG. S1: **Ponderomotive guiding scaling.** Scaling of the inverse electron mean free path (given by Eq. (S8)) as a function of electron confinement factor for various guided electron modes.

of propagation length) at which the electron impinges on the barriers (edges of the trap). Fig. S1 shows the values of $-\text{Im}(2p+1)$ as a function of the confinement $\bar{a} = a/\Delta r_e$, for the first three radial modes. Typical values of $v/2\Omega = 2\pi(v/c)(a^2/\lambda_C)(\Delta r_e/a)^2$ are between tens of microns to millimeters, with $a/\Delta r_e \approx 4.5 - 8$ resulting in extremely long mean free path. However, the latter decreases by orders of magnitude with decreasing confinement, $a/\Delta r_e$.

Finally, Fig. S1 also provides insight into quantifying losses due to coupling mismatch between the electron wavefunction inserted into the fiber and the guided modes. Such mismatch might occur, e.g., due to mismatch in electron beam waist size or due to limited transverse coherence. We can decompose an input wavefunction in the basis of guided modes and estimate such mismatch losses by considering the corresponding reduction in the MFP of the higher-order radial modes.

APPENDIX C: PONDEROMOTIVE GUIDING AND MAXIMAL INTERACTION LENGTH PARAMETERS

In this Appendix, we list the parameters chosen for the ponderomotive traps in each of the examples in the main text. We consider a TE pulse of length $\tau = 100$ psec (0.5 psec), peak power $P_0 = 30$ W (500 W), at wavelength $\lambda_{\text{TE}} = 1200$ nm (610 nm) for the uniform (Bragg) fiber. The position of the modes on the TE01 bands and the mode profiles are illustrated in Fig. 2 and 3.

The maximal fluences of the TE mode we use are 0.9 J/cm² (resp. 0.53 J/cm²) for the uniform fiber (resp., for the Bragg fiber). Such values are within the range of demonstrated pump powers for subwavelength-scale

waveguides fabricated in these materials [43, 44, 61, 70–72] (we note that pump powers could be further reduced at the cost of smaller confinements, which may still be enough for long range guiding – see Appendix B). The resulting guiding energy is found to be $\hbar\Omega = 51.4$ μeV (resp., 325 μeV), with a fundamental guided wavefunction size of $\Delta r_e = 27.2$ nm (resp., 10.8 nm). In both cases, we therefore consider strong localization such that $a/\Delta r_e > 4.5$.

Finally, we consider other limiting factors that constrain the maximal interaction length (see Fig. 4): For the uniform HCNF, $L_{\text{int}} = 4$ cm, corresponding to a GVM length of $L_{\text{GVM}} = 3.6$ cm (calculated from TE group velocity $v_{g,\text{TE}} = 0.4416c$ and electron velocity $v = 0.7c$), and propagation losses of ≈ 0.5 dB/cm (considering tellurite glass nanofibers [42]). For the Bragg fiber, the TE group velocity is matched with the electron velocity, so the only limiting factor is propagation losses, which are taken to be $\approx 0.4 - 3$ dB/cm (SiC nanophotonic waveguides [60]). Hence, we choose to take $L_{\text{int}} = 1$ cm for this example.

APPENDIX D: CALCULATION OF THE FREE-ELECTRON-PHOTON COUPLING

In this Appendix, we provide details on the derivation of the free-electron-photon coupling (g_Q) in the context of this paper. In general, the coupling strength to any mode at wavenumber q can be calculated via the Fourier integral over the z -component of its electric field as

$$g_q = \int d^2\rho \psi_f^*(\rho)\psi_i(\rho) \times \frac{e}{\hbar\omega(q)} \int_0^{L_{\text{int}}} dz e^{-i\frac{\omega(q)}{v}z} E_z^{(s,q)}(\rho, z), \quad (\text{S9})$$

where the index s labels the mode family and band number; v is the electron velocity; and $\psi_{i/f}$ are the initial and final transverse electron wavefunctions. Eq. (S9) is general, and can be converted to expressions commonly found in the literature [1, 4, 37]. In most studies, it is common to assume that $\psi_f \approx \psi_i$ and further that $|\psi_i(\rho)|^2 \approx \delta(\rho)$, treating the electron as a point-like particle in the transverse direction. Below we relax that assumption in order to account for higher-order transitions.

The *total* coupling $|g_Q|$ is often calculated over a discrete set of cavity modes q_j , for which $|g_Q|^2 = \sum_j |g_{q_j}|^2$ [8] or even for a single mode q_0 [1, 4] for which $|g_Q| = |g_{q_0}|$. However, unless stated otherwise, here we consider a continuous spectrum of waveguide modes, for which $|g_Q|^2 = \int dq/2\pi |g_q|^2$. The electric field complex amplitude is $\mathbf{E}^{(s,q)}(\mathbf{r}) = \sqrt{\hbar\omega(q)/2\epsilon_0 A_{s,q}} e^{iqz} \mathbf{u}^{(s,q)}(\mathbf{r})$, where ϵ_0 is the vacuum permittivity, $A_{s,q}$ the mode area, and $\mathbf{u}^{(s,q)}(\mathbf{r})$ the mode function, which is a Bloch function

(along z) for the Bragg (periodic) fiber. For the Bragg fiber, we can further decompose the Bloch function on a Fourier basis as $\mathbf{u}^{(s,q)}(\mathbf{r}) = \sum_m \mathbf{u}_m^{(s,q)}(\boldsymbol{\rho}) e^{i2\pi m z/\Lambda}$, which simplifies to $\mathbf{u}^{(s,q)}(\mathbf{r}) = \mathbf{u}_0^{(s,q)}(\boldsymbol{\rho})$ in the uniform case. In general, only one Fourier order m of the mode's Bloch function contributes to the coupling of a given mode to the electron. Using Eq. (S9) and taking the $dq/2\pi$ integral over all $|g_q|^2$, we find

$$|g_Q|^2 = \frac{\alpha}{\tilde{A}} \frac{L_{\text{int}}}{\lambda} \left| \int d^2 \boldsymbol{\rho} \psi_f^*(\boldsymbol{\rho}) \psi_i(\boldsymbol{\rho}) u_{m,z}^{(s,q_0)}(\boldsymbol{\rho}) \right|^2 \times \int_{-\infty}^{\infty} \frac{dx}{\pi} \text{sinc}^2 \left[\left(1 - \frac{v_g}{v}\right) x - \frac{\omega''}{L_{\text{int}} v} x^2 \right]. \quad (\text{S10})$$

In calculating Eq. (S10), we have assumed that physical quantities such as the mode function and mode area are slowly-varying in q , taking them outside the integral, and evaluating them for a mode at the phase-matching point having a free-space wavelength λ . Furthermore, $\alpha \approx 1/137$ is the fine structure constant, and $\tilde{A} = A/\lambda^2$ is the normalized mode area.

The argument of the sinc function, corresponding to the phase-matching term, was obtained by Taylor expanding $\omega(q)$ around the phase-matching point, up to second order, where v_g is the photonic group velocity and ω'' denotes the second derivative of $\omega(q)$ evaluated at the phase-matching point (this quantity relates to the GVD parameter via $\omega'' = -v_g^3 \beta_2$). The integral in Eq. (S10) takes a closed-form solution for the two types of phase-matching points we consider here: the intersection point (with $v \neq v_g$, neglecting the dispersion $\omega'' \rightarrow 0$) and the tangency point ($v = v_g$ and $\omega'' \neq 0$). Taking the integral in each of these respective limits recovers Eq. (3) of the main text.

The parameters obtained for the TM modes in each of our examples are the following: for the intersection (resp., tangency) phase-matching point, we have electron velocity $v = 0.7c$ (resp., $v = 0.2575c$), TM group velocity $v_{g,\text{TM}} = 0.4124c$ (resp., $v_{g,\text{TM}}$ matched to v), TM wavelength $\lambda_{\text{TM}} = 646.53\text{nm}$ (resp., $\lambda_{\text{TM}} = 423\text{nm}$), normalized TM mode area $\tilde{A} = 0.5175$ (resp., $\tilde{A} = 0.3775$), TM dispersion $\omega'' \approx 0$ (resp., $\omega'' = 87.1\text{m}^2/\text{sec}$), overlap integral with the fundamental electron mode ψ_{00} of $|\int d^2 \boldsymbol{\rho} |\psi_{00}(\boldsymbol{\rho})|^2 u_{0,z}^{(\text{TM})}(\boldsymbol{\rho})| = 0.3487$ (resp., 0.0154 with the $m = 2$ Fourier order), recoil at phase-matching of $q_0 = 1.39 \times 10^7$ (resp., $q_0 + 4\pi/\Lambda = 5.77 \times 10^7 \text{m}^{-1}$), corresponding Kerr nonlinearity of $\kappa = 2\pi \times 1.77\text{GHz}$ (resp., $\kappa = 2\pi \times 30.06 \text{GHz}$), and corresponding nonlinear phase $\delta_{\text{NL}} = 2\kappa(L_{\text{int}}/v) = 1.35\pi$ (resp., $\delta_{\text{NL}} = 15.88\pi$).

APPENDIX E : MODAL ANALYSIS OF HCNF

In this Appendix, we detail the analytical solution of the hollow core nanofiber dispersion and guided mode distribution. We adapt (and generalize) the methods

from, e.g., Refs. [51, 73, 74]. If the permittivity of the structure varies along z , $\epsilon = \epsilon(z)$, it is known that the full fields can be expressed in terms of their z -components [73], which satisfy the following equations:

$$\begin{aligned} \nabla^2 H_z + \epsilon(z) k_0^2 H_z &= 0 \\ \nabla^2 E_z + \epsilon(z) k_0^2 E_z + \frac{\partial}{\partial z} \left(\frac{\epsilon'}{\epsilon} E_z \right) &= 0, \end{aligned} \quad (\text{S11})$$

where $k_0 = \omega/c$ and prime denotes differentiation with respect to z . If the dielectric region is periodic with period Λ , the solutions to the above equations can be expanded in terms of Bessel and Hankel functions of order l and angular momentum $e^{il\phi}$, multiplied by either plane waves $e^{i(q+2\pi m/\Lambda)z}$ (in the vacuum regions) or Bloch waves $e^{iqz} u_{\text{TE},q}^{(m)}(z)$ and $e^{iqz} u_{\text{TM},q}^{(m)}(z)$ (in the periodic dielectric region):

$$\begin{aligned} E_z &= e^{iqz} e^{il\phi} \\ &\times \sum_m \begin{cases} A_m \frac{J_l(\zeta_m \rho)}{J_l(\zeta_m a)} e^{i(2\pi m/\Lambda)z} & \rho \leq a \\ \left[B_m \frac{H_l^{(1)}(\gamma_m \rho)}{H_l^{(1)}(\gamma_m a)} + C_m \frac{H_l^{(2)}(\gamma_m \rho)}{H_l^{(2)}(\gamma_m b)} \right] u_{\text{TM},q}^{(m)}(z) & a \leq \rho \leq b \\ D_m \frac{H_l^{(1)}(\zeta_m \rho)}{H_l^{(1)}(\zeta_m b)} e^{i(2\pi m/\Lambda)z} & \rho \geq b \end{cases} \\ H_z &= \frac{1}{\mu_0 c} e^{iqz} e^{il\phi} \\ &\times \sum_m \begin{cases} E_m \frac{J_l(\zeta_m \rho)}{J_l(\zeta_m a)} e^{i(2\pi m/\Lambda)z} & \rho \leq a \\ \left[F_m \frac{H_l^{(1)}(\gamma_m \rho)}{H_l^{(1)}(\gamma_m a)} + G_m \frac{H_l^{(2)}(\gamma_m \rho)}{H_l^{(2)}(\gamma_m b)} \right] u_{\text{TE},q}^{(m)}(z) & a \leq \rho \leq b \\ H_m \frac{H_l^{(1)}(\zeta_m \rho)}{H_l^{(1)}(\zeta_m b)} e^{i(2\pi m/\Lambda)z} & \rho \geq b \end{cases}, \end{aligned} \quad (\text{S12})$$

where $\zeta_m = \sqrt{k_0^2 - (q + 2\pi m/\Lambda)^2}$, and η_m, γ_m are eigenvalues for the equations satisfied by the Bloch functions [73]:

$$\begin{aligned} [(iq + \partial_z)^2 + \epsilon(z)k_0^2] u_{\text{TE},q}^{(m)} &= \eta_m^2 u_{\text{TE},q}^{(m)} \\ \left[(iq + \partial_z)^2 + \epsilon(z)k_0^2 + (iq + \partial_z) \frac{\epsilon'}{\epsilon} \right] u_{\text{TM},q}^{(m)} &= \gamma_m^2 u_{\text{TM},q}^{(m)} \end{aligned} \quad (\text{S13})$$

The second equation is not self-adjoint, but can be transformed into one if we instead consider modified TM Bloch functions $v_{\text{TM},q}^{(m)} = \sqrt{\epsilon(z)} u_{\text{TM},q}^{(m)}$ which satisfy:

$$\left[(iq + \partial_z)^2 + \epsilon(z)k_0^2 - \sqrt{\epsilon(z)} \left(\frac{1}{\sqrt{\epsilon}} \right)'' \right] v_{\text{TM},q}^{(m)} = \gamma_m^2 v_{\text{TM},q}^{(m)}. \quad (\text{S14})$$

One finds the other field components $E_\phi, E_\rho, H_\phi, H_\rho$ from E_z, H_z by using Maxwell's equations:

$$\begin{aligned} \nabla \times \mathbf{E} &= i\omega \mu_0 \mathbf{H} \\ \nabla \times \mathbf{H} &= -i\omega \epsilon_0 \epsilon(z) \mathbf{E}. \end{aligned} \quad (\text{S15})$$

We then impose a set of boundary conditions on the fields E_z, H_ϕ, H_z, E_ϕ at $\rho = a, b$.

From this set of boundary conditions, a matrix \mathbf{M} of size $8(2N+1)$ -by- $8(2N+1)$ (where $N = 0, 1, 2, \dots$ is the cutoff number of harmonics used in the calculation) is constructed, acting on the vector \mathbf{c} of the $8 \times (2N+1)$ unknown coefficients A_m, B_m, \dots, H_m ($-N \leq m \leq N$), such that $\mathbf{M}\mathbf{c} = 0$. We then numerically solve for the roots $q, \omega(q)$ of the determinant

$$\det \mathbf{M} = 0 \quad (\text{S16})$$

and find the corresponding zero-eigenvector \mathbf{c} of \mathbf{M} that yield the modal functions.

The different mode families are characterized by different OAM numbers l : the TE and TM mode families have $l = 0$, and they occupy separable subspaces having either $E_z = 0$ (with $A_m, \dots, D_m = 0$) or $H_z = 0$ (with $E_m, \dots, H_m = 0$), respectively. The HE and EH mode families have $l \neq 0$, with both E_z, H_z nonzero. A choice of l in our solution can help us “isolate” different mode families.

For better convergence, the abrupt change in $\epsilon(z)$ was replaced with a smooth one using a super-Gaussian function:

$$\epsilon(z) = n_1^2 + (n_2^2 - n_1^2) \exp\{-[(z - \Lambda/2)/\sigma]^p/2\} \quad (\text{S17})$$

with $p = 10$, where the duty cycle is $D = 1 - 2\sigma/\Lambda$. After the effective refractive indices $n_{\text{eff},1}, n_{\text{eff},2}$ are found for n_1 and n_2 , the period and duty cycle are calculated by requiring the quarter-wavelength condition for the desired bandgap wavelength:

$$n_{\text{eff},1}(1 - D)\Lambda = n_{\text{eff},2}D\Lambda = \lambda_{\text{BG}}/4 \quad (\text{S18})$$

Last, we compute the mode area according to:

$$A = \frac{\int d^2\mathbf{r}_T \epsilon(\mathbf{r}_T, z) |E(\mathbf{r}_T, z)|^2}{\max \epsilon(\mathbf{r}_T, z) |E(\mathbf{r}_T, z)|^2} \quad (\text{S19})$$

where, for a uniform HCNF A is constant in z , and for a Bragg HCNF we average $A(z)$ over a unit cell.

APPENDIX F : DERIVATION OF KERR-LIKE HAMILTONIAN IN FREE-ELECTRON-PHOTON INTERACTIONS

In this Appendix, we derive the Hamiltonian describing free-electron-photon interaction. In the case of an electron trapped along a guiding structure (an “electron fiber”), the system is effectively one-dimensional. In the non-relativistic limit, the Hamiltonian is given by:

$$H = \frac{p^2}{2m} + \sum_k \hbar\omega_k a_k^\dagger a_k + \sum_k \hbar\Omega_k (a_k b_k^\dagger + a_k^\dagger b_k), \quad (\text{S20})$$

where $\Omega_k = ev_0 \sqrt{\hbar/2\epsilon_0\omega_k V}$ is the coupling constant for each mode, and $b_k = e^{-ikz}$ is the electron momentum ladder operator, with $[b_k, b_{k'}^\dagger] = 0$ (Ref. [1]). When momentum is conserved, we may make a considerable simplification of the Hamiltonian. Consider the total momentum operator of the electron and field, denoted P :

$$P = p + \sum_k \hbar k a_k^\dagger a_k. \quad (\text{S21})$$

It can be easily shown that this operator is conserved, i.e., $\dot{P} = 0$. Therefore, we may write

$$p = P - \sum_k \hbar k a_k^\dagger a_k, \quad (\text{S22})$$

where P is the operator in the Schrödinger picture (equal to that in the Heisenberg picture at time zero) and write:

$$H = \frac{(P - \sum_k \hbar k a_k^\dagger a_k)^2}{2m} + \sum_k \hbar\omega_k a_k^\dagger a_k + \sum_k \hbar\Omega_k (a_k b_k^\dagger + a_k^\dagger b_k). \quad (\text{S23})$$

We note that there are many initial conditions (e.g., an electron momentum state and any Fock state of the photons) for which the initial state is an eigenstate of P . Any state can be decomposed into eigenstates of this operator. For an eigenstate of this operator, we have that $P = P(0) = \langle \psi(0) | P | \psi(0) \rangle$, which is a *c-number*. This considerably simplifies the Hamiltonian. First, let us expand the Hamiltonian as:

$$H_P = \frac{P^2(0)}{2m} + \sum_k \hbar \left(\omega_k - \frac{kP}{m} + \frac{\hbar k^2}{2m} \right) a_k^\dagger a_k + \sum_k \hbar\Omega_k (a_k b_k^\dagger + a_k^\dagger b_k) + \frac{\hbar^2}{2m} \sum_{k,q} kq a_k^\dagger a_q^\dagger a_q a_k. \quad (\text{S24})$$

In introducing the subscript, we have made it more explicit that the Hamiltonian is parameterized by $P = P(0)$. Next, let us introduce the operator

$$A_k = a_k b_k^\dagger. \quad (\text{S25})$$

Using the commutation relations of b_k , we find that $[A_k, A_{k'}^\dagger] = \delta_{k,k'}$: these new operators have the same commutation relations as photon operators. Using the relation $a_k^\dagger a_k = A_k^\dagger A_k$, therefore, we can write the Hamiltonian as:

$$H = \frac{P^2(0)}{2m} + \sum_k \hbar \left(\omega_k - \frac{kP}{m} + \frac{\hbar k^2}{2m} \right) A_k^\dagger A_k + \sum_k \hbar\Omega_k (A_k + A_k^\dagger) + \frac{\hbar^2}{2m} \sum_{k,q} kq A_k^\dagger A_q^\dagger A_q A_k. \quad (\text{S26})$$

This reformulated Hamiltonian will form the basis for our non-perturbative multiphoton theory nonlinear electron-light interaction. Specifically, in our examples we focus on spontaneous emission, where the initial state is an electron with momentum $p(0) = mv$ and field in the vacuum state $|0\rangle$, which is an eigenstate of P with $P(0) = p(0) = mv$. Substituting this into Eq. (S26), while approximating $k \approx q \approx k_0$ in the nonlinear term (with k_0 denoting the momentum recoil felt by the electron at the phase-matching point), and eliminating the constant energy term $P(0)^2/2m$, we get an effective Kerr Hamiltonian:

$$H_{\text{eff}} = \sum_k \hbar \Delta_k A_k^\dagger A_k + \sum_k \hbar \Omega_k (A_k + A_k^\dagger) + \hbar \kappa N(N-1), \quad (\text{S27})$$

where $\kappa = \hbar k_0^2/2m$ is the effective Kerr nonlinearity,

$$\Delta_k = \omega_k - kv + \frac{\hbar k^2}{2m} \quad (\text{S28})$$

denotes the free-electron-photon detuning and

$$N = \sum_k A_k^\dagger A_k \quad (\text{S29})$$

is the total excitation number. Expanding the detuning around the phase-matching point k_0, ω_0 up to second order, we find

$$\begin{aligned} \Delta_k &\approx (v_g - v + \frac{\hbar}{m} k_0)(k - k_0) + \frac{1}{2} \left(\frac{\hbar}{m} + \omega'' \right) (k - k_0)^2 \\ &\approx (v_g - v)(k - k_0) + \frac{1}{2} \omega'' (k - k_0)^2, \end{aligned} \quad (\text{S30})$$

where $\omega'' = (d^2\omega/dk^2)_{k=k_0}$. As in Appendix D, we can set $v \neq v_g$ and $\omega'' \rightarrow 0$ for an intersection point, and $v = v_g$ with $\omega'' \neq 0$ for a tangency point.

This Hamiltonian can readily deal with initial states which are not eigenstates of P . Let's look at the example of a Gaussian electron wavepacket c_p , centered around some p_0 with momentum uncertainty Δp , coupled to the vacuum state. In this case, our initial wavefunction of the free-electron-photon system, is given by

$$|\psi\rangle = \sum_p c_p |p\rangle |0\rangle. \quad (\text{S31})$$

The evolution of a state $|p\rangle |0\rangle$ is given by the above Hamiltonian, setting $P = p$. Thus, formally one solves $i\hbar\partial_t |\psi\rangle = H_P |\psi\rangle$ for each momentum state. The evolution of the state $|\psi\rangle$ is given by a linear superposition of these individual time evolutions weighted by c_p .

We note, however, that the dynamics could be well-approximated by a Hamiltonian of a single subspace P ,

when certain assumptions are made on the initial electron wavefunction.

First, an electron momentum uncertainty Δp can, in general, cause broadening of the phase-matching bandwidth. This introduces an additive detuning such that $\Delta_k \rightarrow \Delta_k + kp'/m$ (where p' can be of the order of Δp), and accordingly an additional detuning phase-mismatch of the order of $(k\Delta p/m) \times (L/2v)$ (independent of the type of phase-matching point). If this additional detuning is small enough compared to the nonlinearity and if the additional phase mismatch is much smaller than π , we can take $P(0) \approx p_0$ to a very good approximation, integrate the Schrödinger equation and convolve the resulting state with the initial electron wavefunction (such an approach was used to fit theory with experimental data to a very high level of accuracy [7]). Explicitly, in terms of electron energy uncertainty ΔE , this condition reads

$$\frac{\Delta E}{E} \ll \min \left(\frac{\hbar\omega}{2E}, 2\beta \frac{\lambda}{L_{\text{int}}} \right) \quad (\text{S32})$$

where $\lambda = 2\pi c/\omega$ is the free space wavelength and $\beta = v/c$.

Second, we must also assume that we operate in the so-called ‘‘particle-like’’ regime of free-electron-light interaction [37], where the electron's coherent momentum uncertainty Δp is much larger than the phase-matching bandwidth of the considered supermodes. This ensures that individual electron momenta do not get highly-entangled with individual photon momenta *within* a given supermode, as would otherwise occur for plane-waves [75]. In terms of energy uncertainty, this condition reads as

$$\frac{\Delta E}{E} \gg 2 \frac{\lambda_{\text{dB}}}{L_{\text{int}}} \begin{cases} 1/|1 - v_g/v| & \text{intersection} \\ \sqrt{L_{\text{int}}v/\pi\omega''} & \text{tangency} \end{cases} \quad (\text{S33})$$

where $\lambda_{\text{dB}} = h/mv$ is the de Broglie wavelength of the electron. The resulting free-electron-photon entanglement is quasi-discrete (as opposed to a continuous entanglement between free-electron-photon momentum components). Such entanglement manifests as correlations between an optical excitation (e.g., a supermode centered around ω_0) with n photons, and a corresponding electron energy loss peak around $E - n\hbar\omega_0$ [37].

In the following, we shall assume both conditions Eq. (S32) and Eq. (S33) hold, which can be readily achieved in our examples for $\Delta E \leq 0.1\text{eV}$ (and even more so with experimentally-available electron monochromators [76, 77] allowing energy uncertainties down to tens of meV). The aforementioned assumptions allow us to simulate the dynamics through Hamiltonian Eq. (S26), and, if needed, trace out the electron degrees of freedom by taking the trace over the discrete electron energy loss peaks.

APPENDIX G : SUPERMODE ANALYSIS OF FREE-ELECTRON-PHOTON NONLINEAR DYNAMICS

In this Appendix, we derive a supermode theory of our nonlinear dynamics. Supermodes are typically used to describe quantum nonlinear dynamics in multimode systems, such as synchronously-pumped optical parametric oscillator [78]. We write the Heisenberg equations for A_k as:

$$\dot{A}_k = -i\Delta_k A_k - 2i\kappa N A_k - i\Omega_k^*. \quad (\text{S34})$$

In this equation, the nonlinear term is proportional to the total excitation number and is therefore invariant upon unitary transformation on the mode basis. We can thus choose a supermode basis, represented by wavepacket operators

$$w_n(t) = \int dk \tilde{w}_n(k) e^{i\Delta_k t} A_k(t), \quad (\text{S35})$$

where the $\tilde{w}_n(k)$'s are an orthonormal, complete basis of wavepackets, such that $\sum_n w_n^\dagger w_n = \int dk A_k^\dagger A_k = N$. The supermodes satisfy the following dynamics

$$\dot{w}_n = -2i\kappa w_n - i s_n(t) \quad (\text{S36})$$

with driving terms given by

$$s_n(t) = \int dk \Omega_k^* e^{i\Delta_k t} \tilde{w}_n(k). \quad (\text{S37})$$

We first consider linear dynamics ($\kappa = 0$) over interaction time T (with time $t \in [-T/2, T/2]$). At $t = T/2$, the field populates a *single* supermode, denoted as w_0 , with wavepacket

$$\tilde{w}_0(k) = \frac{\Omega_k T}{|g_Q|} \text{sinc} \frac{\Delta_k T}{2} \quad (\text{S38})$$

such that $w_n(T/2) = w_n(-T/2) - i|g_Q|\delta_{n,0}$, recovering a known result of the quantum theory of the photon-induced near field electron microscopy effect, which uses instead the scattering matrix formalism [1, 4].

In the presence of the nonlinear term $\kappa \neq 0$, the dynamics may be described by multiple supermodes or approach that of a single supermode, depending on the type of phase-matching point considered. In any case, in the following we shall consider an orthonormal basis of wavepackets containing $\tilde{w}_0(k)$, wherein most of the energy should still be contained.

The general procedure for finding the supermode basis $\{\tilde{w}_n\}$ is the following: choose an orthonormal basis $\{\tilde{\psi}_n\}$, containing a basis vector $\tilde{\psi}_0$ which maximally overlaps with \tilde{w}_0 (or that's identical to it, in which case $\{\tilde{w}_n\} \equiv \{\tilde{\psi}_n\}$). If necessary, one can construct $\{\tilde{w}_n\}$ from $\{\tilde{\psi}_n\}$ and $\{\tilde{\psi}_n\}/\{\tilde{\psi}_0\}$ using a Gram-Schmidt process. Then,

calculate an auxiliary set of driving terms for the $\{\tilde{\psi}_n\}$ basis, given by

$$\bar{s}_n(t) = \int dk \Omega_k^* e^{i\Delta_k t} \tilde{\psi}_n(k) \quad (\text{S39})$$

from which the sources for the dynamics of w_n of Eq. (S35) could be readily inferred via

$$s_n(t) = \sum_m \langle \tilde{\psi}_m | \tilde{w}_n \rangle \bar{s}_m(t), \quad (\text{S40})$$

where $(\cdot | \cdot)$ denotes inner product between complex functions.

We now outline the different examples, and consider $\Omega_k = \Omega$ uniform, for simplicity. Whenever needed, we use the auxiliary Hermite function basis

$$\tilde{\psi}_n(k) = \frac{1}{\sqrt{2^n n! \sqrt{\pi} \sigma}} e^{-k^2/2\sigma^2} H_n\left(\frac{k}{\sigma}\right), \quad (\text{S41})$$

find the scale σ for which the overlap between $\tilde{\psi}_0(k)$ and $\tilde{w}_0(k)$ is maximal, and proceed according to the procedure above.

Phase-matching to a mode continuum. First, consider phase-matching to a continuum of modes in a waveguide. For an intersection point, with linear dispersion $\Delta_k = \delta v k$ (where $\delta v = v_e - v_g$), we find

$$\bar{s}_n(t) = \frac{|g_Q|}{T} \frac{i^n \sqrt{2\sigma'}}{\sqrt{2^n n! \sqrt{\pi}}} \exp\left[-\frac{1}{2} \left(\sigma' \frac{2t}{T}\right)^2\right] H_n\left(\sigma' \frac{2t}{T}\right) \quad (\text{S42})$$

where $\sigma' = \sigma \delta v T/2 \approx 1.4$ is the optimal scaling for the intersection point. In deriving $\bar{s}_n(t)$ we used the identity

$$\int_{-\infty}^{\infty} dx e^{ixt} e^{-x^2/2} H_n(x) = \sqrt{2\pi} i^n e^{-t^2/2} H_n(t). \quad (\text{S43})$$

For a tangency point, with quadratic dispersion $\Delta_k = \omega'' k^2/2$, we find

$$\begin{aligned} \bar{s}_{2n}(t) &= \frac{|g_Q|}{T} \frac{(2n)!}{\sqrt{2^{2n} (2n)! n!}} \sqrt{\frac{3}{2}} \sigma' \\ &\times \frac{\exp\left[i(2n + \frac{1}{2}) \arctan(2\sigma'^2 \frac{2t}{T})\right]}{\left[1 + (2\sigma'^2 \frac{2t}{T})^2\right]^{\frac{1}{4}}}, \end{aligned} \quad (\text{S44})$$

where $\bar{s}_{2n+1}(t) = 0$, and this time $\sigma' = \sigma \sqrt{\omega'' T}/2 = \sqrt{\sqrt{3}/2} \approx 0.93$ is the optimal scaling. In deriving $\bar{s}_n(t)$ we used the identity

$$\int_{-\infty}^{\infty} dx e^{-cx^2} H_{2n}(x) = \sqrt{\frac{\pi}{c}} \frac{(2n)!}{n!} \left(\frac{1-c}{c}\right)^n, \quad \text{Re}(c) > 0. \quad (\text{S45})$$

Phase-matching to a discrete set of cavity modes. Now, consider the phase matching to a discrete set of cavity

modes $k_j = (\pi/L)j$, where L is the cavity length. In that case, the dispersion is

$$\Delta_j = \delta v \frac{\pi}{L} j = \frac{\pi v_e}{L} \left(1 - \frac{v_g}{v_e}\right) j \equiv \Delta j, \quad (\text{S46})$$

and the fundamental supermode is

$$\tilde{w}_0(j) = \frac{\Omega T}{|g_Q|} \text{sinc} \left[\left(1 - \frac{v_g}{v_e}\right) \frac{\pi}{2} j \right], \quad (\text{S47})$$

where we assumed that the electron traverses the full length of the cavity such that $T = L/v_e$, and introduced the effective free spectral range (FSR)

$$\Delta = \frac{\pi v_e}{L} \left(1 - \frac{v_g}{v_e}\right). \quad (\text{S48})$$

approaching the true FSR for $|v_e| \ll |v_g|$. Next, we consider the special case where

$$1 - \frac{v_g}{v_e} = 2m, \quad (\text{S49})$$

for an integer m other than 0, for which $\Delta = 2\pi m/T$ and

$$\tilde{w}_0(j) = \frac{\Omega T}{|g_Q|} \delta_{j,0}. \quad (\text{S50})$$

In that case, our supermode basis $\{\tilde{w}_n(j)\}$ coincides with the cavity mode basis $\{\delta_{j,n}\}$ - as it is already a complete orthonormal basis containing \tilde{w}_0 , and we can readily calculate the driving terms as

$$s_n(t) = \frac{|g_Q|}{T} \exp\left(in \frac{2\pi m}{T} t\right) \quad (\text{S51})$$

Finally, the nonlinear cavity dynamics can take two limiting forms: when the nonlinear detuning 2κ is an integer multiple of Δ , after each recoil the electron becomes phase-matched to a neighbouring cavity mode, and thus cascaded phase-matching to different cavity modes can occur. However, if the detuning 2κ is a half-integer multiple of Δ , then after a single recoil, the electron is maximally-detuned from neighbouring modes:

$$2\kappa = \begin{cases} n\Delta & \text{cascade} \\ (n + 1/2)\Delta & \text{maximal detuning} \end{cases} \quad (\text{S52})$$

where in the maximally-detuned case, the limits of $m \gg 1$ (or $v_e \ll v_g$) and $\delta_{\text{NL}} = 2\kappa T \gg 2\pi$ reduce to the single-mode Jaynes-Cummings interaction for slow electrons [11]. Both cases are illustrated in Fig. 5 of the main text.

FUNDING

A.K. is supported by the VATAT-Quantum fellowship by the Israel Council for Higher Education; the Urbanek-Chodorow postdoctoral fellowship by the Department of

Applied Physics at Stanford University; the Zuckerman STEM leadership postdoctoral program; and the Viterbi fellowship by the Technion. C. R.-C. is supported by a Stanford Science Fellowship. N.R. acknowledges the support of a Junior Fellowship from the Harvard Society of Fellows. S. F. acknowledges the support from the Department of Energy. (Grant No. DE-FG02-07ER46426).

ACKNOWLEDGMENTS

The authors acknowledge fruitful discussions with Ido Kaminer and Zhexin Zhao.

DISCLOSURES

The authors declare no conflict of interest.

DATA AVAILABILITY

Data may be obtained from the authors upon reasonable request.

* Electronic address: karnieli@stanford.edu

† Electronic address: chrc@stanford.edu

- [1] O. Kfir, "Entanglements of Electrons and Cavity Photons in the Strong-Coupling Regime," *Physical Review Letters*, vol. 123, p. 103602, 9 2019.
- [2] V. Di Giulio, M. Kociak, and F. J. G. de Abajo, "Probing quantum optical excitations with fast electrons," *Optica*, vol. 6, p. 1524, 12 2019.
- [3] A. Gover and A. Yariv, "Free-Electron-Bound-Electron Resonant Interaction," *Physical Review Letters*, vol. 124, p. 064801, 2 2020.
- [4] A. Ben Hayun, O. Reinhardt, J. Nemirovsky, A. Karnieli, N. Rivera, and I. Kaminer, "Shaping quantum photonic states using free electrons," *Science Advances*, vol. 7, pp. 4270–4280, 3 2021.
- [5] R. Ruimy, A. Gorlach, C. Mechel, N. Rivera, and I. Kaminer, "Toward Atomic-Resolution Quantum Measurements with Coherently Shaped Free Electrons," *Physical Review Letters*, vol. 126, p. 233403, 6 2021.
- [6] Z. Zhao, X. Q. Sun, and S. Fan, "Quantum Entanglement and Modulation Enhancement of Free-Electron-Bound-Electron Interaction," *Physical Review Letters*, vol. 126, p. 233402, 6 2021.
- [7] R. Dahan, A. Gorlach, U. Haeusler, A. Karnieli, O. Eyal, P. Yousefi, M. Segev, A. Arie, G. Eisenstein, P. Hommelhoff, and I. Kaminer, "Imprinting the quantum statistics of photons on free electrons," *Science*, vol. 373, 9 2021.
- [8] A. Feist, G. Huang, G. Arend, Y. Yang, J. W. Henke, A. S. Raja, F. J. Kappert, R. N. Wang, H. Lourenço-Martins, Z. Qiu, J. Liu, O. Kfir, T. J. Kippenberg, and C. Ropers, "Cavity-mediated electron-photon pairs," *Science*, vol. 377, pp. 777–780, 8 2022.

- [9] R. Dahan, G. Baranes, A. Gorlach, R. Ruimy, N. Rivera, and I. Kaminer, “Creation of Optical Cat and GKP States Using Shaped Free Electrons,” *Physical Review X*, vol. 13, p. 031001, 6 2023.
- [10] Y. Adiv, H. Hu, S. Tsesses, R. Dahan, K. Wang, Y. Kurman, A. Gorlach, H. Chen, X. Lin, G. Bartal, I. Kaminer, and E. Viterbi, “Observation of 2D Cherenkov Radiation,” *Physical Review X*, vol. 13, p. 011002, 1 2023.
- [11] A. Karnieli and S. Fan, “Jaynes-Cummings interaction between low-energy free electrons and cavity photons,” *Science advances*, vol. 9, p. eadh2425, 6 2023.
- [12] O. Reinhardt, C. Mechel, M. Lynch, and I. Kaminer, “Free-Electron Qubits,” *Annalen der Physik*, vol. 533, p. 2000254, 2 2021.
- [13] M. V. Tsarev, A. Ryabov, and P. Baum, “Free-electron qubits and maximum-contrast attosecond pulses via temporal Talbot revivals,” *Physical Review Research*, vol. 3, p. 043033, 12 2021.
- [14] G. Baranes, R. Ruimy, A. Gorlach, and I. Kaminer, “Free electrons can induce entanglement between photons,” *npj Quantum Information* 2022 8:1, vol. 8, pp. 1–9, 3 2022.
- [15] A. Karnieli, S. Tsesses, R. Yu, N. Rivera, A. Arie, I. Kaminer, and S. Fan, “Universal and ultrafast quantum computation based on free-electron-polariton blockade,” *PRX Quantum*, vol. 5, p. 010339, 3 2024.
- [16] G. Baranes, S. Even-Haim, R. Ruimy, A. Gorlach, R. Dahan, A. A. Diringer, S. Hacohe-Gourgy, and I. Kaminer, “Free-electron interactions with photonic GKP states: Universal control and quantum error correction,” *Phys. Rev. Research*, vol. 5, p. 043271, 3 2023.
- [17] A. Gorlach, A. Karnieli, R. Dahan, E. Cohen, A. Pe’er, and I. Kaminer, “Ultrafast non-destructive measurement of the quantum state of light using free electrons,” *arXiv:2012.12069*, 12 2020.
- [18] A. Karnieli, S. Tsesses, R. Yu, N. Rivera, Z. Zhao, A. Arie, S. Fan, and I. Kaminer, “Quantum sensing of strongly coupled light-matter systems using free electrons,” *Science advances*, vol. 9, p. eadd2349, 1 2023.
- [19] T. Bucher, H. Nahari, H. H. Sheinfux, R. Ruimy, A. Niedermayr, R. Dahan, Q. Yan, Y. Adiv, M. Yannai, J. Chen, Y. Kurman, S. T. Park, D. J. Masiel, E. Janzen, J. H. Edgar, F. Carbone, G. Bartal, S. Tsesses, F. H. L. Koppens, G. M. Vanacore, and I. Kaminer, “Coherently amplified ultrafast imaging in a free-electron interferometer,” *arXiv:2305.04877*, 5 2023.
- [20] T. Bucher, R. Ruimy, S. Tsesses, R. Dahan, G. Bartal, G. M. Vanacore, and I. Kaminer, “Free-Electron Ramsey-Type Interferometry for Enhanced Amplitude and Phase imaging of Nearfields,” *Sci. Adv.*, vol. 9, p. eadi5729, 5 2023.
- [21] X. Bendaña, A. Polman, and F. J. García De Abajo, “Single-photon generation by electron beams,” *Nano Letters*, vol. 11, pp. 5099–5103, 12 2011.
- [22] V. Di Giulio and F. J. García De Abajo, “Optical-cavity mode squeezing by free electrons,” *Nanophotonics*, vol. 11, pp. 4659–4670, 12 2022.
- [23] N. Talebi, “Strong Interaction of Slow Electrons with Near-Field Light Visited from First Principles,” *Physical Review Letters*, vol. 125, p. 080401, 8 2020.
- [24] M. Eldar, Z. Chen, Y. Pan, and M. Krüger, “Self-Trapping of Slow Electrons in the Energy Domain,” *Physical Review Letters*, vol. 132, p. 035001, 1 2024.
- [25] Y. Pan, B. Zhang, and D. Podolsky, “Low-energy Free-electron Rabi oscillation and its applications,” *arXiv:2304.12174*, 4 2023.
- [26] F. J. García De Abajo, E. J. Dias, and V. Di Giulio, “Complete Excitation of Discrete Quantum Systems by Single Free Electrons,” *Physical Review Letters*, vol. 129, p. 093401, 8 2022.
- [27] A. P. Synanidis, P. A. D. Gonçalves, C. Ropers, and F. J. G. de Abajo, “Quantum effects in the interaction of low-energy electrons with light,” *arXiv:2403.09896*, 3 2024.
- [28] S. Tsesses, G. Bartal, and I. Kaminer, “Light generation via quantum interaction of electrons with periodic nanostructures,” *Physical Review A*, vol. 95, p. 013832, 1 2017.
- [29] S. Huang, R. Duan, N. Pramanik, J. Scott Herrin, C. Boothroyd, Z. Liu, . Liang, and J. Wong, “Quantum recoil in free-electron interactions with atomic lattices,” *Nature Photonics* 2023, pp. 1–7, 1 2023.
- [30] D. E. Chang, V. Vuletić, and M. D. Lukin, “Quantum nonlinear optics — photon by photon,” *Nature Photonics* 2014 8:9, vol. 8, pp. 685–694, 8 2014.
- [31] S. E. Korbly, A. S. Kesar, J. R. Sirigiri, and R. J. Temkin, “Observation of Frequency-Locked Coherent Terahertz Smith-Purcell Radiation,” *Phys. Rev. Lett.*, vol. 94, p. 054803, 2005.
- [32] M. Shentcis, A. K. Budniak, X. Shi, R. Dahan, Y. Kurman, M. Kalina, H. Herzig Sheinfux, M. Blei, M. K. Svendsen, Y. Amouyal, S. Tongay, K. S. Thygesen, F. H. Koppens, E. Lifshitz, F. J. García de Abajo, L. J. Wong, and I. Kaminer, “Tunable free-electron X-ray radiation from van der Waals materials,” *Nature Photonics*, vol. 14, pp. 686–692, 11 2020.
- [33] A. Polman, M. Kociak, and F. J. García de Abajo, “Electron-beam spectroscopy for nanophotonics,” *Nature Materials*, vol. 18, p. 1158–1171, 7 2019.
- [34] F. J. García de Abajo and V. Di Giulio, “Optical Excitations with Electron Beams: Challenges and Opportunities,” *ACS Photonics*, vol. 17, p. 36, 4 2021.
- [35] C. Roques-Carmes, S. E. Kooi, Y. Yang, N. Rivera, P. D. Keathley, J. D. Joannopoulos, S. G. Johnson, I. Kaminer, K. K. Berggren, and M. Soljačić, “Free-electron–light interactions in nanophotonics,” *Applied Physics Reviews*, vol. 10, p. 011303, 1 2023.
- [36] M. Bézard, I. S. H. Mohand, L. Ruggiero, A. L. Roux, Y. Auad, P. Baroux, L. H. G. Tizei, X. Chécoury, and M. Kociak, “High efficiency coupling of free electrons to sub- λ^3 modal volume, high-Q photonic cavities,” *arXiv:2307.15556*, 7 2023.
- [37] G. Huang, N. J. Engelsen, O. Kfir, C. Ropers, and T. J. Kippenberg, “Electron-Photon Quantum State Heralding Using Photonic Integrated Circuits,” *PRX Quantum*, vol. 4, p. 020351, 6 2023.
- [38] Y. D’Mello, S. Bernal, X. Shi, I. Kaminer, R. Dahan, and D. V. Plant, “Efficient coupling between free electrons and the supermode of a silicon slot waveguide,” *Optics Express*, Vol. 31, Issue 12, pp. 19443–19452, vol. 31, pp. 19443–19452, 6 2023.
- [39] B. J. Brenny, T. Coenen, and A. Polman, “Quantifying coherent and incoherent cathodoluminescence in semiconductors and metals,” *Journal of Applied Physics*, vol. 115, p. 244307, 6 2014.
- [40] A. Massuda, C. Roques-Carmes, Y. Yang, S. E. Kooi, Y. Yang, C. Murdia, K. K. Berggren, I. Kaminer, and M. Soljačić, “Smith-Purcell Radiation from Low-Energy Electrons,” *ACS Photonics*, vol. 5, pp. 3513–3518, 9 2018.

- [41] D. Roitman, D. Roitman, A. Karnieli, S. Tsesses, Z. Barkay, A. Arie, and A. Arie, “Coherent radiation at visible wavelengths from sub-keV electron beams,” *Optics Letters*, Vol. 49, Issue 8, pp. 2013–2016, vol. 49, pp. 2013–2016, 4 2024.
- [42] Q. Yang, J. He, J. Qiu, J. Zhang, Z. Ye, J. Lou, Y. Shen, L. Tong, and L. Hu, “Photonic nanowires directly drawn from bulk glasses,” *Optics Express*, Vol. 14, Issue 1, pp. 82–87, vol. 14, pp. 82–87, 1 2006.
- [43] M. Liao, W. Gao, Z. Duan, X. Yan, T. Suzuki, Y. Ohishi, S. G. Leon-Saval, T. A. Birks, W. J. Wadsworth, P. J. St Russell, M. W. Mason, D. I. Yeom, E. C. Mägi, M. R. E Lamont, M. A. F Roelens, L. Fu, and B. J. Eggleton, “Directly draw highly nonlinear tellurite microstructured fiber with diameter varying sharply in a short fiber length,” *Optics Express*, Vol. 20, Issue 2, pp. 1141–1150, vol. 20, pp. 1141–1150, 1 2012.
- [44] Y. Ohishi, M. Liao, X. Xue, T. Cheng, Z. Duan, T. Suzuki, and W. Gao, “Flat and broadband supercontinuum generation by four-wave mixing in a highly nonlinear tapered microstructured fiber,” *Optics Express*, Vol. 20, Issue 26, pp. B574–B580, vol. 20, pp. B574–B580, 12 2012.
- [45] Z. Xie, Z. Chen, H. Li, Q. Yan, H. Chen, X. Lin, I. Kaminer, O. D. Miller, and Y. Yang, “Maximal quantum interaction between free electrons and photons,” *arXiv:2404.00377*, 3 2024.
- [46] V. Di Giulio, E. Akerboom, A. Polman, and F. J. G. de Abajo, “Toward Optimum Coupling between Free Electrons and Confined Optical Modes,” *arXiv:2403.15823*, 3 2024.
- [47] Z. Zhao, “Upper bound for the quantum coupling between free electrons and photons,” *arXiv:2404.01221*, 4 2024.
- [48] A. Goban, C. L. Hung, J. D. Hood, S. P. Yu, J. A. Muniz, O. Painter, and H. J. Kimble, “Superradiance for Atoms Trapped along a Photonic Crystal Waveguide,” *Physical Review Letters*, vol. 115, p. 063601, 8 2015.
- [49] G. Epple, K. S. Kleinbach, T. G. Euser, N. Y. Joly, T. Pfau, P. S. J. Russell, and R. Löw, “Rydberg atoms in hollow-core photonic crystal fibres,” *Nature Communications* 2014 5:1, vol. 5, pp. 1–5, 6 2014.
- [50] E. Shahmoon, G. Kurizki, M. Fleischhauer, and D. Petrosyan, “Strongly interacting photons in hollow-core waveguides,” *Physical Review A - Atomic, Molecular, and Optical Physics*, vol. 83, p. 033806, 3 2011.
- [51] H. Ito, K. Sakaki, T. Nakata, W. Jhe, and M. Ohtsu, “Optical potential for atom guidance in a cylindrical-core hollow fiber,” *Optics Communications*, vol. 115, pp. 57–64, 3 1995.
- [52] R. Zimmermann, M. Seidling, and P. Hommelhoff, “Charged particle guiding and beam splitting with autoponderomotive potentials on a chip,” *Nature Communications* 2021 12:1, vol. 12, pp. 1–6, 1 2021.
- [53] J. Hammer, S. Thomas, P. Weber, and P. Hommelhoff, “Microwave chip-based beam splitter for low-energy guided electrons,” *Physical Review Letters*, vol. 114, p. 254801, 6 2015.
- [54] L. Schächter and W. D. Kimura, “Electron beam guiding by a laser Bessel beam,” *Physical Review Accelerators and Beams*, vol. 23, p. 081301, 8 2020.
- [55] R. J. England, R. J. Noble, K. Bane, D. H. Dowell, C. K. Ng, J. E. Spencer, S. Tantawi, Z. Wu, R. L. Byer, E. Peralta, K. Soong, C. M. Chang, B. Montazeri, S. J. Wolf, B. Cowan, J. Dawson, W. Gai, P. Hommelhoff, Y. C. Huang, C. Jing, C. McGuinness, R. B. Palmer, B. Naranjo, J. Rosenzweig, G. Travish, A. Mizrahi, L. Schachter, C. Sears, G. R. Werner, and R. B. Yoder, “Dielectric laser accelerators,” *Reviews of Modern Physics*, vol. 86, pp. 1337–1389, 12 2014.
- [56] A. Hanuka and L. Schächter, “Trapping of sub-relativistic particles in laser driven accelerators,” *Physics of Plasmas*, vol. 24, p. 123116, 12 2017.
- [57] R. Shiloh, N. Schönenberger, N. Schönenberger, Y. Adiv, Y. Adiv, R. Ruimy, R. Ruimy, A. Karnieli, A. Karnieli, A. Karnieli, T. Hughes, R. J. England, K. J. Leedle, D. S. Black, Z. Zhao, P. Musumeci, R. L. Byer, A. Arie, I. Kaminer, I. Kaminer, P. Hommelhoff, and P. Hommelhoff, “Miniature light-driven nanophotonic electron acceleration and control,” *Advances in Optics and Photonics*, Vol. 14, Issue 4, pp. 862–932, vol. 14, pp. 862–932, 12 2022.
- [58] R. Shiloh, J. Illmer, T. Chlouba, P. Yousefi, N. Schönenberger, U. Niedermayer, A. Mittelbach, and P. Hommelhoff, “Electron phase-space control in photonic chip-based particle acceleration,” *Nature* 2021 597:7877, vol. 597, pp. 498–502, 9 2021.
- [59] F. J. García de Abajo, “Optical excitations in electron microscopy,” *Reviews of Modern Physics*, vol. 82, no. 1, pp. 209–275, 2010.
- [60] A. Yi, C. Wang, L. Zhou, Y. Zhu, S. Zhang, T. You, J. Zhang, and X. Ou, “Silicon carbide for integrated photonics,” *Applied Physics Reviews*, vol. 9, p. 31302, 9 2022.
- [61] H. Tezuka, Y. Ohishi, X. Xue, T. Cheng, M. Matsumoto, T. Suzuki, T. H. Tuan, and K. Nagasaka, “Mid-infrared supercontinuum generation spanning 2.0 to 15.1 μm in a chalcogenide step-index fiber,” *Optics Letters*, Vol. 41, Issue 9, pp. 2117–2120, vol. 41, pp. 2117–2120, 5 2016.
- [62] A. S. Sheremet, M. I. Petrov, I. V. Iorsh, A. V. Poshakinskiy, and A. N. Poddubny, “Waveguide quantum electrodynamics: Collective radiance and photon-photon correlations,” *Reviews of Modern Physics*, vol. 95, p. 015002, 1 2023.
- [63] M. Jankowski, R. Yanagimoto, E. Ng, R. Hamerly, T. P. McKenna, H. Mabuchi, and M. M. Fejer, “Ultrafast second-order nonlinear photonics – from classical physics to non-Gaussian quantum dynamics,” *arXiv:2401.06265*, 1 2024.
- [64] Y. Yang, C. Roques-Carmes, S. E. Kooi, H. Tang, J. Beroz, E. Mazur, I. Kaminer, J. D. Joannopoulos, and M. Soljačić, “Photonic flatband resonances for free-electron radiation,” *Nature* 2023 613:7942, vol. 613, pp. 42–47, 1 2023.
- [65] B. Temelkuran, S. D. Hart, G. Benoit, J. D. Joannopoulos, and Y. Fink, “Wavelength-scalable hollow optical fibres with large photonic bandgaps for CO₂ laser transmission,” *Nature* 2003 420:6916, vol. 420, pp. 650–653, 12 2002.
- [66] J. D. Joannopoulos, S. G. Johnson, J. N. Winn, and R. D. Meade, *Photonic Crystals : Molding the Flow of Light (Second Edition)*. Princeton University Press, 2008.
- [67] J. Lim, S. Kumar, Y. S. Ang, L. K. Ang, and L. J. Wong, “Quantum Interference between Fundamentally Different Processes Is Enabled by Shaped Input Wavefunctions,” *Advanced Science*, p. 2205750, 2023.
- [68] E. Arqué López, V. Di Giulio, and F. J. García De Abajo, “Atomic Floquet physics revealed by free electrons,” *Physical Review Research*, vol. 4, p. 013241, 3 2022.

- [69] J. Hu and C. R. Menyuk, “Understanding leaky modes: slab waveguide revisited,” *Advances in Optics and Photonics*, Vol. 1, Issue 1, pp. 58-106, vol. 1, pp. 58–106, 1 2009.
- [70] V. V. Dorofeev, M. P. Smayev, V. V. Koltashev, Y. P. Yatsenko, and A. G. Okhrimchuk, “Nonlinear properties of the depressed cladding single mode TeO₂-WO₃-Bi₂O₃ channel waveguide fabricated by direct laser writing,” *Optical Materials Express*, Vol. 8, Issue 11, pp. 3424-3437, vol. 8, pp. 3424–3437, 11 2018.
- [71] G. L. DesAutels, C. Brewer, S. Juhl, P. Powers, M. Walker, S. Ristich, M. Whitaker, and M. Finet, “Femtosecond laser damage threshold and nonlinear characterization in bulk transparent SiC materials,” *JOSA B*, Vol. 25, Issue 1, pp. 60-66, vol. 25, pp. 60–66, 1 2008.
- [72] J. Cardenas, M. Yu, A. L. Gaeta, Y. Okawachi, M. Lipson, R. K. W. Lau, C. B. Poitras, and A. Dutt, “Optical nonlinearities in high-confinement silicon carbide waveguides,” *Optics Letters*, Vol. 40, Issue 17, pp. 4138-4141, vol. 40, pp. 4138–4141, 9 2015.
- [73] X. Gao, B. Zhen, M. Soljačić, H. Chen, and C. W. Hsu, “Bound States in the Continuum in Fiber Bragg Gratings,” *ACS Photonics*, vol. 6, pp. 2996–3002, 11 2019.
- [74] Govind P. Agrawal, *Fiber-optic communication systems*. fourth edition ed., 2021.
- [75] A. Karnieli, N. Rivera, A. Arie, and I. Kaminer, “The coherence of light is fundamentally tied to the quantum coherence of the emitting particle,” *Science Advances*, vol. 7, p. eabf8096, 4 2021.
- [76] O. L. Krivanek, N. Dellby, J. A. Hachtel, J. C. Idrobo, M. T. Hotz, B. Plotkin-Swing, N. J. Bacon, A. L. Bleloch, G. J. Corbin, M. V. Hoffman, C. E. Meyer, and T. C. Lovejoy, “Progress in ultrahigh energy resolution EELS,” *Ultramicroscopy*, vol. 203, pp. 60–67, 8 2019.
- [77] M. Yannai, Y. Adiv, R. Dahan, K. Wang, A. Gorlach, N. Rivera, T. Fishman, M. Krüger, and I. Kaminer, “Lossless Monochromator in an Ultrafast Electron Microscope Using Near-Field THz Radiation,” *Physical Review Letters*, vol. 131, p. 145002, 10 2023.
- [78] G. J. De Valcárcel, G. Patera, N. Treps, and C. Fabre, “Multimode squeezing of frequency combs,” *Physical Review A - Atomic, Molecular, and Optical Physics*, vol. 74, p. 061801, 12 2006.
- [79] We note that the β -factor for free-electron-photon coupling was also named “coupling ideality” in the literature [37].